Cell

Mitochondrial Cristae Shape Determines Respiratory Chain Supercomplexes Assembly and Respiratory Efficiency

Sara Cogliati,[1,2] Christian Frezza,[1] Maria Eugenia Soriano,[1,2] Tatiana Varanita,[1,2] Ruben Quintana-Cabrera,[1,2] Mauro Corrado,[1,3] Sara Cipolat,[1] Veronica Costa,[1] Alberto Casarin,[4] Ligia C. Gomes,[1] Ester Perales-Clemente,[5] Leonardo Salviati,[4] Patricio Fernandez-Silva,[6] Jose A. Enriquez,[5,*] and Luca Scorrano[1,2,3,*]

[1]Dulbecco-Telethon Institute, Venetian Institute of Molecular Medicine, Via Orus 2, 35129 Padova, Italy
[2]Department of Biology, University of Padova, Via U. Bassi 58B, 35121 Padova, Italy
[3]IRCCS Fondazione Santa Lucia, Via Ardeatina 306, 00143 Rome, Italy
[4]Clinical Genetics Unit, Department of Woman and Child Health, University of Padova, Via Giustiniani 3, 35128 Padova, Italy
[5]Centro Nacional de Investigaciònes Cardiovasculares Carlos III, Melchor Fernàndez Almagro 3, 28029 Madrid, Spain
[6]Departamento de Bioquìmica y Biologia Molecular y Celular, Facultad de Ciencias, Universidad de Zaragoza, Pedro Cerbuna 12, 50009 Zaragoza, Spain
*Correspondence: jaenriquez@cnic.es (J.A.E.), luca.scorrano@unipd.it (L.S.)
http://dx.doi.org/10.1016/j.cell.2013.08.032

SUMMARY

Respiratory chain complexes assemble into functional quaternary structures called supercomplexes (RCS) within the folds of the inner mitochondrial membrane, or cristae. Here, we investigate the relationship between respiratory function and mitochondrial ultrastructure and provide evidence that cristae shape determines the assembly and stability of RCS and hence mitochondrial respiratory efficiency. Genetic and apoptotic manipulations of cristae structure affect assembly and activity of RCS in vitro and in vivo, independently of changes to mitochondrial protein synthesis or apoptotic outer mitochondrial membrane permeabilization. We demonstrate that, accordingly, the efficiency of mitochondria-dependent cell growth depends on cristae shape. Thus, RCS assembly emerges as a link between membrane morphology and function.

INTRODUCTION

Mitochondria are key organelles in intermediate cellular metabolism, energy conversion, and calcium homeostasis (Dimmer and Scorrano, 2006). They also integrate and amplify apoptosis induced by intrinsic stimuli, releasing cytochrome *c* and other proapoptotic factors required for the activation of caspases (Green and Kroemer, 2004). Cytochrome *c* release is regulated by proteins of the BCL-2 family that control the permeabilization of the outer membrane (OMM) (Danial and Korsmeyer, 2004).

Energy conversion occurs at the inner mitochondrial membrane (IMM) that can be further divided into two subcompartments: the so-called "boundary membrane" and the cristae, separated from the former by narrow tubular junctions (Frey and Mannella, 2000). The cristae shape is dynamic: upon activation of mitochondrial respiration, "orthodox" mitochondria become "condensed," with an expanded cristae space (Hackenbrock, 1966). During apoptosis, the curvature of the cristae membrane is inverted in a remodeling process required for the complete release of cytochrome *c*, normally confined in the cristae (Scorrano et al., 2002; Frezza et al., 2006; Yamaguchi et al., 2008). Cristae remodeling occurs in response to proapoptotic BH3-only BCL-2 family members, such as BID, BIM-S, and BNIP3, and independently of the outer membrane multidomain BCL-2 family members BAX and BAK (Scorrano et al., 2002; Cipolat et al., 2006; Yamaguchi et al., 2008). Whether changes in morphology of the cristae, where respiratory chain complexes (RCCs) mainly localize (Vogel et al., 2006), affect oxidative phosphorylation efficiency, as originally predicted (Hackenbrock, 1966), is unclear. This issue is further complicated by the assembly of RCC in supercomplexes (RCS) (Schägger, 1995; Acín-Pérez et al., 2008), quaternary supramolecular structures that, by channeling electrons among individual RCCs, allow the selective use of RCC subsets for nicotine adenine dinucleotide (NADH)- or flavin adenine dinucleotide-derived electrons (Lapuente-Brun et al., 2013). Such a supramolecular organization is common in cristae: also, the mitochondrial ATP synthase is assembled into dimers with greater adenosine triphosphatase (ATPase) activity (Campanella et al., 2008; Gomes et al., 2011). Interestingly, cristae shape and ATPase dimers are linked: in yeast mutants where the ATPase cannot dimerize, cristae are disorganized (Paumard et al., 2002; Minauro-Sanmiguel et al., 2005; Strauss et al., 2008), whereas in mammalian cells, increased cristae density favors ATPase dimerization during autophagy (Gomes et al., 2011). On the contrary, despite their importance in mitochondrial bioenergetics,

the relationship between RCS and cristae shape remains unclear.

Mitochondrial morphology and ultrastructure depends on "mitochondria-shaping" proteins that regulate organellar fusion and fission (Griparic and van der Bliek, 2001). Mitofusins (MFN) 1 and 2, highly homologous dynamin-related proteins of the OMM, orchestrate fusion (Santel and Fuller, 2001; Legros et al., 2002; Chen et al., 2003; Santel et al., 2003). MFN1 primarily participates in fusion, cooperating with the IMM dynamin-related protein optic atrophy 1 (OPA1) (Cipolat et al., 2004), whereas MFN2 also tethers mitochondria to the endoplasmic reticulum (de Brito and Scorrano, 2008). Mitochondrial fission is regulated by the cytoplasmic dynamin-related protein 1 that, upon calcineurin-dependent dephosphorylation, translocates to mitochondria (Yoon et al., 2001; Smirnova et al., 2001; Cereghetti et al., 2008). Genetic depletion of OPA1 leads to disorganization of the cristae (Frezza et al., 2006), and oligomers that contain a soluble and a membrane-bound form of OPA1 keep the cristae junctions tight, independently from OPA1 role in fusion (Frezza et al., 2006; Cipolat et al., 2006). During apoptosis, these oligomers are early targets of BID, BIM-S, and BNIP3, as well as of intrinsic death stimuli (Frezza et al., 2006; Yamaguchi et al., 2008; Landes et al., 2010; Costa et al., 2010). Whereas our knowledge of the molecular determinants of cristae shape and their role in apoptosis is increasing, the relationship between cristae morphology and mitochondrial function remains unexplored. We therefore set out to genetically dissect whether and how cristae shape regulates mitochondrial respiration. We show that cristae morphology determines assembly and stability of RCS and hence optimal mitochondrial respiratory function during life and death of the cell.

RESULTS

Genetic Dissection of Outer Membrane Permeabilization from Cristae Remodeling

Whether apoptotic cristae remodeling that maximizes cytochrome *c* release from mitochondria affects mitochondrial function is unclear, mainly because it occurs around the same time as outer membrane permeabilization (Scorrano et al., 2002). In order to genetically dissociate the two processes, we inspected the primary structure of the prototypical cristae remodeling inducer BCL-2 family member BID for homology with peptides known to perturb the mitochondrial inner membrane, like mastoparan, a 14 amino acid wasp venom component (Pfeiffer et al., 1995). Interestingly, BID membrane inserting α6 helix as well as the transmembrane domains of Bnip3 and BimS that also remodel cristae (Yamaguchi et al., 2008; Landes et al., 2010) displayed homology to mastoparan (Figures S1A and S1B available online). To exploit the role of this homologous sequence in cristae remodeling, we mutagenized the two highly conserved 157 and 158 Lys *H. sapiens* BID residues to Ala (BID^{KKAA}) (Figure S1C). Because this mutation did not impair caspase-8 cleaved recombinant BID (cBID) integration in purified mouse liver mitochondria (MLM) (Wei et al., 2000; Figure S1D), we could measure its biological activity using an established quantitative, specific cytochrome *c* release ELISA (Scorrano et al., 2002). cBID efficiently released cytochrome *c* from purified mitochondria, whereas a BH3 domain G94E mutant was, as expected, inactive (Wei et al., 2000) and the $cBID^{KKAA}$ mutant released ~25%–30% more cytochrome *c* than the baseline (Figure 1A), a figure close to the amount of free intermembrane space cytochrome *c* (Scorrano et al., 2002). BAK oligomerization was superimposable in cBID or $cBID^{KKAA}$-treated mitochondria (Figure 1B); conversely, two established assays of intramitochondrial cytochrome *c* redistribution, the cytochrome b_5-dependent extramitochondrial NADH oxidation and the ratio of ascorbate-driven over tetramethyl-p-phenylenediamine (TMPD)-driven respiration (Scorrano et al., 2002), indicated that $cBID^{KKAA}$ mobilized the cristae cytochrome *c* pool less efficiently than cBID (Figures 1C and 1D). Indeed, $cBID^{KKAA}$ was unable to remodel mitochondrial cristae, as indicated by morphometric analysis of electron micrographs of mitochondria treated with the BID mutants (Figures 1E and 1F) (Scorrano et al., 2002). Cristae remodeling is associated with the disruption of high molecular weight (HMW) OPA1 oligomers (Frezza et al., 2006). Western blots of blue native gel electrophoresis (BNGE) of mitochondrial proteins revealed four major OPA1-containing complexes. Upon treatment with cBID, OPA1 rapidly disappeared from ~720 kDa HMW complexes (Figures 1G, S1E, and S1F). These HMW forms of OPA1 were similarly targeted by $cBID^{G94E}$ but significantly less by $cBID^{KKAA}$, as determined by BNGE (Figure 1H, quantification in [I]). Chemical crosslinking experiments (Frezza et al., 2006) further confirmed that the OPA1-containing oligomer is disrupted by the mutants of cBID able to induce cristae remodeling (Figures S1G and S1H). Finally, we measured the killing efficiency of these truncated BID (tBID) mutants expressed in mouse embryonic fibroblasts (MEFs). Only tBID efficiently killed MEFs: $tBID^{KKAA}$ and $tBID^{G94E}$ elicited comparable low levels of cell death, whereas the double $tBID^{KKAA,G94E}$ mutant appeared completely ineffective (Figure 1J), suggesting that both outer membrane permeabilization and mitochondrial cristae remodeling are required for BID-induced apoptosis. In conclusion, BID^{KKAA} is deficient in cristae remodeling, cytochrome *c* release, and induction of apoptosis.

RCS Disassemble during Cristae Remodeling

The BID^{KKAA} mutant dissociates outer membrane permeabilization from cristae remodeling and can be used to investigate the relationship between the latter and mitochondrial function. We therefore measured the effect of the BID mutants on the respiratory control ratio (RCR), an index of respiratory efficiency, of mitochondria incubated with excess exogenous cytochrome *c* and NADH (to compensate for the potential effects of inner membrane or outer membrane [OM] permeabilization). cBID reduced RCR only when mitochondria were energized with substrates for complex I (glutamate/malate) but not when they were fed with substrates entering the electron transport chain at complex II (succinate) or complex IV (ascorbate + TMPD) (Figure 2A; data not shown). Interestingly, these changes were recapitulated by the BH3 domain mutant $cBID^{G94E}$ that does not permeabilize the OM but not by the cristae remodeling-deficient mutants $cBID^{KKAA}$ and $cBID^{KKAA,G94E}$ (Figure 2B). Maximal (uncoupled) respiration was similarly affected by the cBID mutants tested, ruling out that BID alters RCR, because it affects ATPase or activity or ATP/ADP exchange (Figure S2A). These experiments

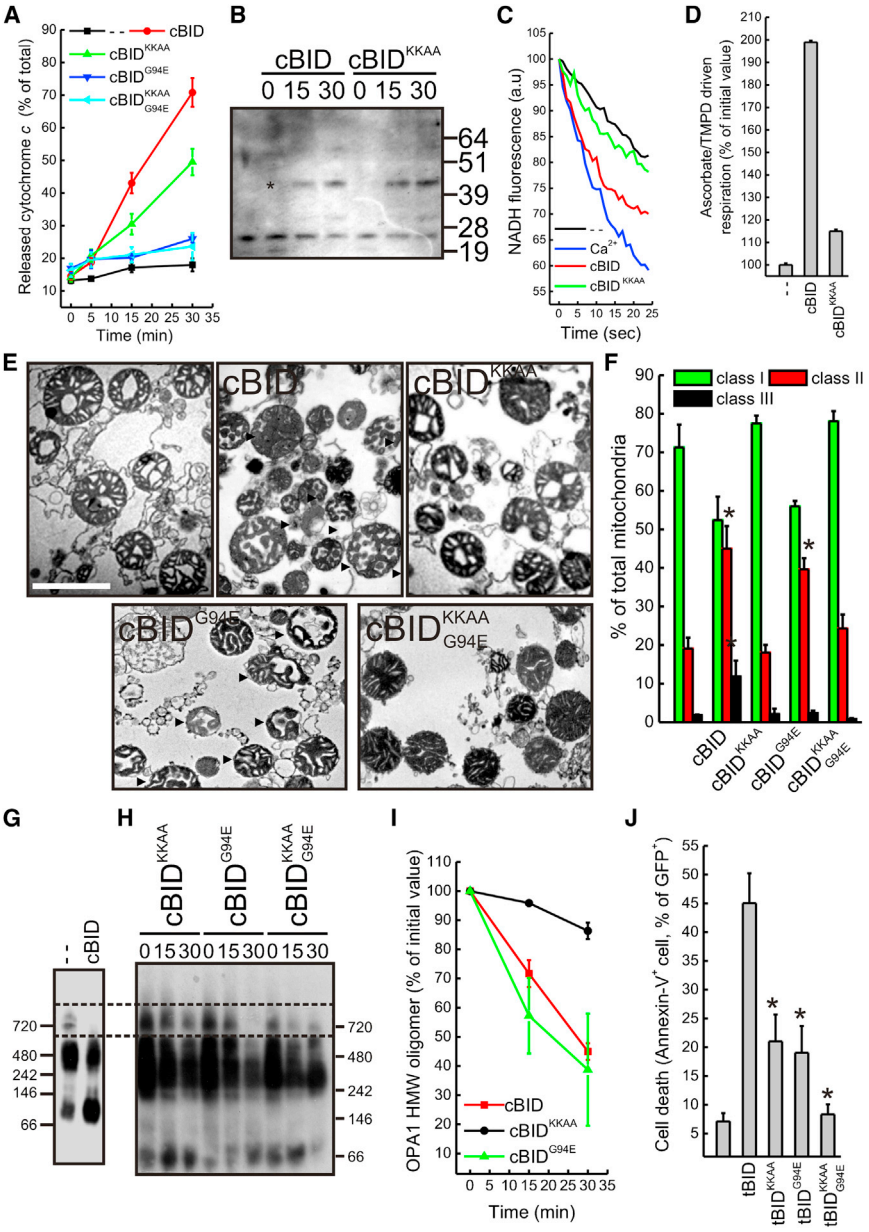

Figure 1. Two Conserved Lys in BID α6 Helix Are Required for Cristae Remodeling

(A) Mitochondria were treated for the indicated times with the indicated mutants of cBID, and cytochrome *c* release was measured by ELISA. Data represent average ± SEM of five independent experiments.

(B) Mitochondria treated with the indicated mutants of cBID for the indicated min were cross-linked with 1 mM BMH for 30 min, spun, and the pellets were separated by SDS-PAGE and immunoblotted using anti-BAK antibody. The asterisks denote BAK oligomers.

(C) Mitochondria were treated as indicated (Ca^{2+}, 200 μM), and cytochrome b_5-dependent NADH fluorescence changes were recorded. a.u., arbitrary units.

(D) Mitochondria were treated for 15 min with the indicated BID mutants, transferred into the chamber of a Clark's type O_2 electrode, and the ascorbate/TMPD-driven respiration ratio was determined. Data represent average ± SEM of four independent experiments.

(E) Representative electron microscopy fields of mitochondria treated for 15 min with the indicated cBID mutants. Arrows indicate class II and III mitochondria. The scale bar represents 450 nm.

(F) Blind morphometric analysis of randomly selected EM of mitochondria treated with the indicated cBID mutants (as in [E]). Mitochondria were assigned to morphological classes I–III as in Scorrano et al. (2002). Data represent average ± SEM of three independent experiments. The asterisk denotes $p < 0.05$ in a paired sample Student's t test versus untreated.

(G and H) BNGE analysis of OPA1 oligomers in MLM treated for 30 min (G) or for the indicated minutes (H), as indicated. The boxed area indicates the HMW complexes of OPA1.

(I) Densitometric analysis of OPA1 HMW complexes. Experiments were as in (H). Data represent average ± SEM of four independent experiments.

(J) MEFs were transfected with the pMIG plasmid containing the indicated insert and after 48 hr cell death was determined cytofluorimetrically as the percentage of Annexin-V^+, GFP^+ cells. Data represent average ± SEM of four independent experiments. The asterisk denotes $p < 0.05$ in a paired sample Student's t test versus tBID.

See also Figure S1.

suggest that cristae remodeling causes complex I-dependent changes in mitochondrial bioenergetics.

Complex I is further assembled in quaternary functional RCS with complexes III and IV (I + III and I + III + IV), whereas most complex II is not found in RCS (Acín-Pérez et al., 2008). Thus, the reduction in complex I-supported respiration could be a consequence of specific inhibition of complex I or of issues in RCS function. Even after 30 min of acute BID treatment, the specific complex I NADH-ubiquinone reductase activity of purified mitochondria was unaltered (data not shown), prompting us to investigate RCS assembly and stability in situ. We therefore took advantage of *Bax*$^{-/-}$, *Bak*$^{-/-}$ (DKO) MEFs, resistant to mitochondrial permeabilization, cytochrome *c* release, and apoptosis triggered by expression of tBID (Wei et al., 2001). Upon transduction of metabolically labeled DKO MEFs with tBID but not with $tBID^{KKAA}$ that does not cause cristae remodeling (Figure S2B), the RCS radioactivity signal as well as the RCS/complex V radioactivity ratio were reduced (Figures 2C and 2D), and we observed a reduction in the autoradiographic signal of cytochrome *b* retrieved in RCS compared to that in free complex III (Figures 2E and 2F). Whereas this result could suggest that complex III was incorporated less efficiently into RCS, immunoblotting for the complex I subunit NDUFA9 revealed that RCSs were also destabilized in DKO cells (Figure 2G). Functionally, only cBID and $cBID^{G94E}$ that cause cristae remodeling but not $cBID^{KKAA}$ reduced glutamate-supported RCR in DKO mitochondria (Figure 2H). Thus, BID destabilizes RCS and selectively reduces glutamate-dependent RCR.

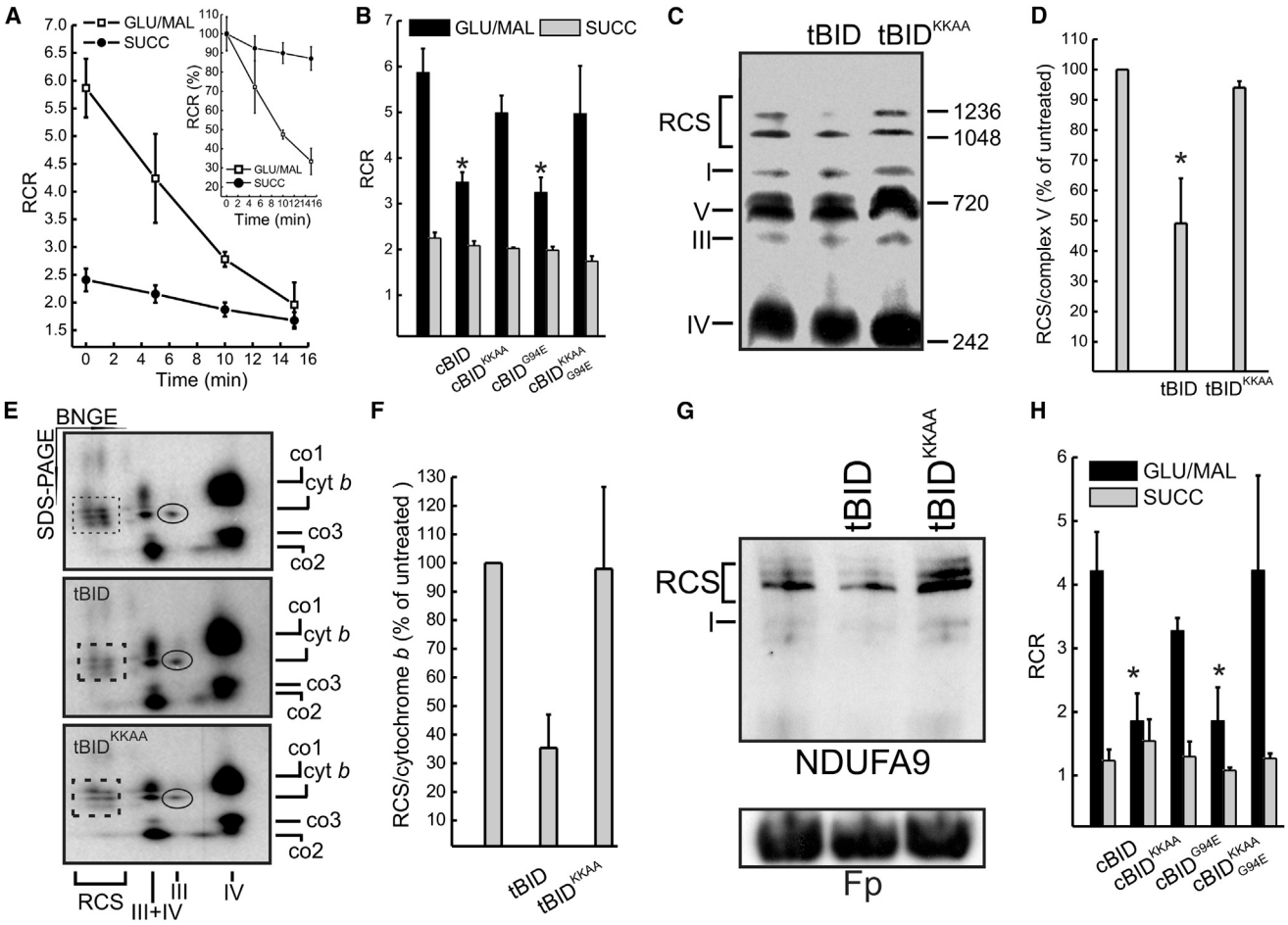

Figure 2. Respiratory Chain Supercomplexes Are Disassembled during Cristae Remodeling

(A) RCR of mitochondria energized with 5 mM/2.5 mM glutamate/malate (GLU/MAL) or 10 mM succinate (SUCC) treated for the indicated times with cBID. Data represent average ± SEM of five independent experiments. Inset, RCR values normalized to t = 0.

(B) Experiments were as in (A), except that mitochondria were incubated with the indicated mutants of cBID for 15 min. Data represent average ± SEM of four independent experiments. The asterisk denotes $p < 0.05$ in a paired sample Student's t test versus untreated.

(C) BNGE of mitochondrial OXPHOS protein from DKO MEFs transduced as indicated and, after 2 days, metabolically labeled for 2 hr and lysed after 24 hr. Equal amounts of protein (100 μg) were separated by BNGE, and radioactivity was detected in the fixed and dried gels for 1 week. RCC and RCS of the respiratory chain are indicated.

(D) Densitometric analysis of the autoradiographic RCS/complex V signal ratio. Data represent average ± SEM of three independent experiments performed as in (E). The asterisk denotes $p < 0.05$ in a paired sample Student's t test versus untreated.

(E) 2D BN/SDS PAGE analysis of mitochondrial OXPHOS proteins from DKO MEFs transduced as indicated, metabolically labeled for 2 hr, and lysed after 24 hr. Equal amount (50 μg) of proteins were separated in native condition, and then the lanes were excised and proteins separated by a second dimension SDS-PAGE. The gels were dried and the signal was detected following 1 week of exposure. RCC and RCS of the respiratory chain as well as the single-labeled proteins are indicated. Boxes and circles indicate RCS and cytochrome *b*, respectively.

(F) Densitometric analysis of the ratio of autoradiographic signal between supercomplex (boxed) and complex assembled cytochrome *b* (circled). Data represent average ± SEM of three independent experiments. The asterisk denotes $p < 0.05$ in a paired sample Student's t test versus untreated.

(G) BNGE analysis of OXPHOS proteins in mitochondria from DKO MEFs transduced as indicated. Equal amounts (100 μg) of proteins were separated in native conditions, transferred onto PVDF membranes, and probed with the indicated antibodies. RCC and RCS are indicated.

(H) RCR of DKO mitochondria energized with 5 mM/2.5 mM GLU/MAL or 10 mM SUCC treated for 15 min with the indicated cBID mutants. Data represent average ± SEM of four independent experiments. The asterisk denotes $p < 0.05$ in a paired sample Student's t test versus untreated.

See also Figure S2.

Conditional Ablation of *Opa1* Alters Cristae Shape and RCS Assembly

To verify whether RCS disorganization was a general consequence of altered cristae shape, we turned to cells lacking *Opa1*, a key regulator of cristae morphology (Frezza et al., 2006). However, chronic *Opa1* depletion impaired mitochondrial DNA (mtDNA) levels and translation (Figures S3A and S3B), complicating the analysis of the relationship between *Opa1* and RCS and calling for a model of conditional *Opa1* ablation. We produced, by homologous recombination, C57BL6/J

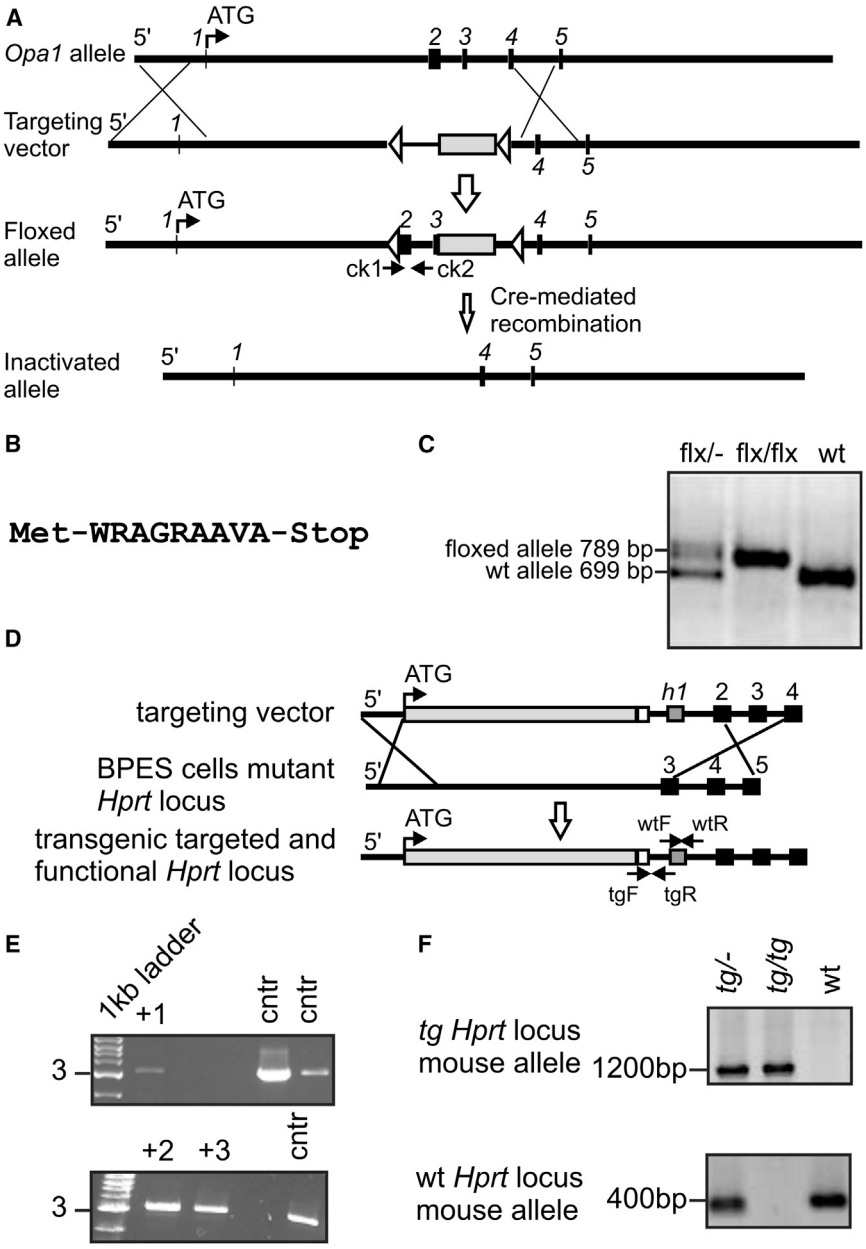

Figure 3. Generation of *Opa1*$^{flx/flx}$ and *Opa1*^{tg} Mice

(A) Maps of the wild-type *Opa1* allele, the targeting vector, the conditional floxed allele, and the inactivated *Opa1* allele. The 5′ UTR, exons (black boxes), LoxP sites (white arrows), FRT recombination sites, and PGK-neomycin cassette (white box) are indicated. The locations of PCR primers (*ck1 = primer check1 forward, ck2 = primer check2 reverse*) are indicated. Dimensions are not in scale.

(B) Prediction of the maximal possible aberrant OPA1 protein.

(C) RT-PCR analysis of transcripts in heterozygous (flx/−), homozygous (flx/flx), and WT mice.

(D) Maps of the targeting vector, the mutant *Hprt* locus of BPES cells, and the transgenic targeted and functional *Hprt* locus. The 5′ UTR, the human *β-ACTIN* promoter and *Opa1* gene (light gray box), poly A (white box), *human* exon 1 of *Hprt* locus (*h1*, dark gray box), and *Hprt* locus exons (black boxes) are indicated. The locations of PCR primers (WTF, WT forward; WTR, WT reverse; tgF, transgenic forward; tgR, transgenic reverse) are indicated. Dimensions are not in scale.

(E) RT-PCR screening of ESC clones. The positive clones are indicated.

(F) RT-PCR analysis of transcripts in heterozygous (tg/−), homozygous (tg/tg), and WT mice.

See also Figure S3.

embryonic stem cells with loxP sites inserted in the *Opa1* gene (*Opa1*$^{flx/flx}$), which were then microinjected in C57BL6/J blastocysts to generate *Opa1*$^{flx/flx}$ mice. Following Cre-mediated recombination, the deletion of exons 2 and 3 resulted in an aberrant exon1–exon4 transcript with a stop codon immediately after exon 1, producing a predicted 10 amino acid (aa) residual protein (Figures 3A and 3B). Chimerism and germ-line transmission of the offspring was tested by PCR, and germ-line transmittants were bred to homozygosity (Figure 3C). Fibroblasts isolated from the diaphragm of homozygous *Opa1*$^{flx/flx}$ 7-week-old male mice (MAFs) were immortalized and used for subsequent analysis. OPA1 was completely ablated 24 hr after adenoviral delivery of Cre recombinase (Figure 4A) and, as expected, mitochondria were fragmented (Figures 4B and 4C) with defects in cristae shape (Figures 4D and 4E). Four days after Cre-mediated *Opa1* ablation, mtDNA copy number (Figure 4F) and translation (Figures 4G and 4H) were unaffected, allowing us to specifically address the role of OPA1 and cristae shape in RCS assembly using an assay based on the incorporation of radiolabeled mtDNA-encoded proteins into RCC and RCS (Acín-Pérez et al., 2008). Upon acute *Opa1* ablation, the assembly of mtDNA-encoded subunits into RCC was not affected (data not shown). We therefore followed the RCS assembly rate (measured as the ratio between RCS and complex V radioactivity throughout the chase period) that resulted ~8-fold slower when Opa1 was ablated from *Opa1*$^{flx/flx}$ MAFs (Figures 4I and 4J). A similar reduction in the RCS assembly rate was observed in *Opa1*$^{-/-}$ MEFs (Figure S3C), suggesting that, in absence of *Opa1*, RCC are less superassembled, irrespective of their initial levels. To test if acute *Opa1* ablation altered RCS in vivo, we tail vein-injected Cre-expressing adenoviruses in *Opa1*$^{flx/flx}$ animals. After 72 hr, OPA1 levels in liver mitochondria were reduced by ~50% (Figure S4A), cristae morphology was abnormal (Figure S4B), RCS were reduced (Figure S4C), and glutamate/malate RCR was impaired (Figure 4K). These experiments of conditional ablation of *Opa1* identify a role for cristae shape in RCS assembly in vitro and in vivo.

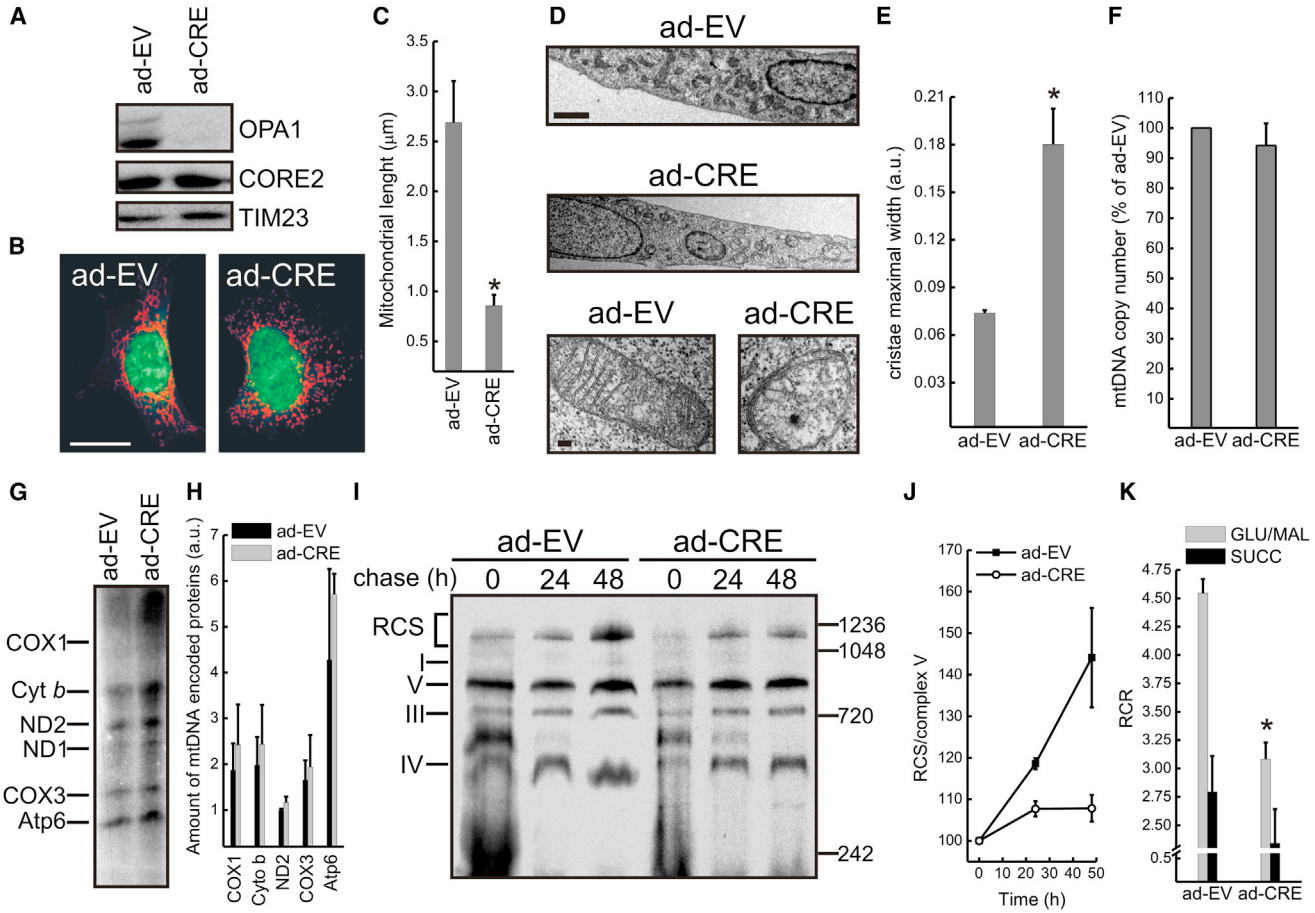

Figure 4. Acute Ablation of *Opa1* Alters Mitochondrial Morphology, Cristae Shape, and RCS Assembly

(A) *Opa1*$^{flx/flx}$ MAFs were infected with bicistronic adenoviruses carrying the indicated insert (EV, empty vector; CRE, Cre recombinase) upstream of GFP and, after 24 hr, equal amounts of proteins (20 μg) were separated by SDS-PAGE and immunoblotted with the indicated antibodies.

(B) *Opa1*$^{flx/flx}$ MAFs were infected with the indicated adenoviruses and, after 24 hr, fixed, immunostained using an anti-TOM20 antibody, and representative confocal images acquired. The green cytoplasmic staining identifies the coexpression of GFP. The scale bar represents 20 μm.

(C) Average mitochondrial major axis length. Experiments were as in (B). Data represent average ± SEM of four independent experiments (five mitochondria per cell, at least 50 cells/experiment). The asterisk denotes $p < 0.05$ in a paired sample Student's t test versus ad-EV.

(D) *Opa1*$^{flx/flx}$ MAFs were infected with the indicated adenoviruses and, after 24 hr, fixed and processed for electron microscopy. The scale bars represent 2 μm (top) and 200 nm (bottom).

(E) Morphometric analysis of cristae width in 40 randomly selected mitochondria of *Opa1*$^{flx/flx}$ MAFs infected with the indicated adenoviruses. Data represent average ± SEM of three independent experiments. The asterisk denotes $p < 0.05$ in a paired sample Student's t test versus ad-EV.

(F) Mitochondrial DNA copy number quantification. mtDNA was amplified by RT-PCR from total DNA of *Opa1*$^{flx/flx}$ MAFs infected with the indicated adenoviruses. Data are normalized to MAFs infected with control adenovirus and represent average ± SEM of four independent experiments.

(G) mtDNA translation assay. *Opa1*$^{flx/flx}$ MAFs infected as indicated were metabolic labeled in presence of emetine and lysed after 30 min. Protein samples (40 μg) were separated by SDS-PAGE, and the radioactivity was detected in the fixed and dried gels for 3 days. The mtDNA encoded proteins are indicated.

(H) Densitometric analysis of the mtDNA-encoded proteins. Experiments are as in (G). Data represent average ± SEM of four independent experiments.

(I) RCS assembly assay. *Opa1*$^{flx/flx}$ MAFs were infected as indicated and, after 24 hr, metabolically labeled for 2 hr and then chased for the indicated times. Equal amounts of protein (100 μg) were separated by BN PAGE, and radioactivity was detected in the fixed and dried gels for 1 week. RCC and RCS of the respiratory chain are indicated.

(J) Densitometric analysis of the incorporation rate of radioactivity into supercomplexes. Values are normalized for the autoradiographic signal of complex V. Data represent average ± SEM from three independent experiments performed as in (H).

(K) RCR of mitochondria isolated from livers of *Opa1*$^{flx/flx}$ mice 3 days after tail-vein injection of the indicated adenoviruses, energized with 5 mM/2.5 mM GLU/MAL or 10 mM SUCC. Data represent average ± SEM of four independent experiments. The asterisk denotes $p < 0.05$ in a paired sample Student's t test versus ad-EV.

See also Figure S4.

Overexpression of *Opa1* Increases RCS Assembly

The model linking cristae shape to RCS predicts that higher OPA1 levels should favor RCS assembly. To verify this hypothesis, we wanted to generate a mouse model of *Opa1* overexpression. Very high OPA1 levels are, however, toxic, causing paradoxical mitochondrial fragmentation (Cipolat

et al., 2004): we therefore targeted, by homologous recombination in the murine X chromosome *Hprt* region, a transgene-carrying mouse variant 1 *Opa1* under the human *β-actin* promoter (*Opa1*^{tg}) (Figure 3D). The integration into microinjected BPES embryonic stem cells was verified by PCR (Figure 3E), and the cells were microinjected into C57BL6/J blastocysts. Six generated agouti chimeras with a chimerism exceeding 90% were bred with C57BL6/J mates and tested for germline transmission by fur color and transgene PCR analysis (Figure 3F). Mice were viable, fertile, grew normally, and resisted to different forms of tissue damage (T.V., M.E.S., V. Romanello, S.C., V.C., R. Menabò, M. Sandri, F. Di Lisa, and L.S., unpublished data). Immortalized MAFs prepared from the diaphragm of hemizygous *Opa1*^{tg} 7-week-old C57BL6/J male mice displayed an ~1.5 increase in OPA1 levels compared to age- and sex-matched littermate controls MAFs (wild-type [WT]; Figure 5A). Mitochondria were slightly elongated (Figures 5B and 5C) and cristae tighter (Figures 5D and 5E), without any difference in mtDNA levels (Figure 5F) and translation (Figures 5G and 5H). Importantly, in *Opa1*^{tg} MAFs, RCS assembly (Figures 5I and 5J) and glutamate-supported RCR (Figure 5K) were increased. In vivo, an ~50% increase in liver mitochondria OPA1 levels (Figure S5A) was similarly associated to tighter cristae (Figure S5B) and increased RCS levels (Figure S5C). Taken together, these results indicate that RCS assembly is facilitated by increased OPA1 levels and tighter cristae.

Mitochondria-Supported Cell Growth Is Controlled by Cristae Shape

We next wished to address if cristae shape affects mitochondrial-dependent cell growth. We therefore measured the growth of DKO cells (resistant to BID-induced outer membrane permeabilization, caspase-dependent mitochondrial damage, and apoptosis) in galactose media, where most of cellular ATP comes from the respiratory chain (Acín-Pérez et al., 2004). WT and G94E tBID impaired growth in galactose, whereas cells transduced with tBID^{KKAA} that does not cause cristae remodeling did not display any defect (Figure 6A).

We next turned to genetic models of cristae shape changes. Growth in galactose-containing media was impaired upon acute ablation of *Opa1* in MAFs, whereas it was normal for fusion-deficient *Mfn1*$^{-/-}$, *Mfn2*$^{-/-}$ MEFs (Figures 6B and 6C), where mitochondrial fusion is also inhibited. In *Mfn1*$^{-/-}$, *Mfn2*$^{-/-}$ MEFs, mtDNA copy number was reduced (Figure S6A), but cristae shape (Figures S6B and S6C), mtDNA translation (Figure S6D), RCS stability (Figure S6E), and assembly (Figure S6F) were not affected. Thus, the galactose growth defect is not the consequence of impaired fusion but correlates with altered cristae shape and RCS. Finally, *Opa1*^{tg} MAFs grew faster than their WT counterparts in galactose media (Figure 6D), further confirming the link between cristae shape, RCS levels, and mitochondria-dependent cellular growth. In conclusion, cristae shape correlates with the efficiency of mitochondria-dependent cell growth.

DISCUSSION

Respiratory chain supercomplexes have been considered BNGE artifacts until direct respirometric experiments on purified RCS identified them as the functional mitochondrial respiratory units (Acín-Pérez et al., 2008). Since then, RCS have been directly visualized in intact cristae by electron tomography (Davies et al., 2011), complex IV assembly factors that favor RCS formation have been identified (Chen et al., 2012; Vukotic et al., 2012; Strogolova et al., 2012; Lapuente-Brun et al., 2013), and the role of RCS in mitochondrial utilization of reducing equivalents has been demonstrated (Lapuente-Brun et al., 2013). However, the relationship between cristae shape and RCS, as well as between RCS and mitochondrial function, remained obscure. Our results demonstrate that cristae shape regulates respiratory chain supercomplexes stability and assembly, impacting on respiratory efficiency and respiratory cell growth.

To dissect the role of cristae shape in RCS structure and function, we genetically ablated the master cristae shape regulator OPA1. Individual respiratory chain units associate with OPA1 (Zanna et al., 2008), and mitochondrial metabolism is deranged in dominant optic atrophy caused by *OPA1* mutations (Lodi et al., 2004). However, the defect in ATP production in *OPA1* haploinsufficient cells was unexplained: OPA1 is not essential for assembly of respiratory chain complexes and mtDNA levels as well as activities of individual respiratory chain complexes are normal in dominant optic atrophy (Zanna et al., 2008). Conversely, the reduction in mtDNA copy number has been invoked to explain the mitochondrial dysfunction of fusion-deficient cells from *Mfn1*, *Mfn2*-deficient mice (Chen et al., 2010). Our results challenge this hypothesis: upon acute *Opa1* ablation, mtDNA levels are normal, whereas cristae shape, RCS, complex-I-dependent respiration, and respiratory growth are impaired. Conversely, in *Mfn1*$^{-/-}$, *Mfn2*$^{-/-}$ cells, mtDNA copy number is reduced, but cristae shape, RCS, and respiratory growth are normal. Thus, RCS disorganization shall be regarded as a key mechanism of mitochondrial dysfunction accompanying altered organelle morphology.

The role of OPA1 and cristae shape in RCS organization is further supported by mouse models of *Opa1* conditional ablation and mild overexpression. The first tool allowed us to dissociate cristae biogenesis from mtDNA maintenance: whereas chronic *Opa1* depletion reduces mtDNA copy number and translation, upon acute *Opa1* ablation, mtDNA levels are normal, but cristae are disorganized, impacting on RCS assembly and respiratory function and growth. Thus, mtDNA reduction appears to be a consequence of chronic fusion inhibition in *Opa1*$^{-/-}$ (and double *Mfn*$^{-/-}$) cells. We can therefore predict that the *Opa1*$^{flx/flx}$ cells will be useful to elucidate how prolonged inhibition of mitochondrial fusion results in mtDNA levels reduction. *Opa1* mild overexpression lends further support to the model linking RCS organization to cristae shape: RCS assembly and respiratory function and growth are increased in *Opa1*^{tg} cells without any measurable change in mtDNA levels and translation. The *Opa1*^{tg} mouse will be instrumental to investigate the role of *Opa1* and cristae shape in vivo.

Apoptotic cristae remodeling further supports the relationship between cristae shape and RCS. The role and mechanisms of cristae remodeling in apoptosis are controversial (Scorrano et al., 2002; Germain et al., 2005; Frezza et al., 2006; Yamaguchi et al., 2008; Merkwirth et al., 2008; Costa et al., 2010). Despite that OPA1-mediated stabilization of cristae shape inhibits

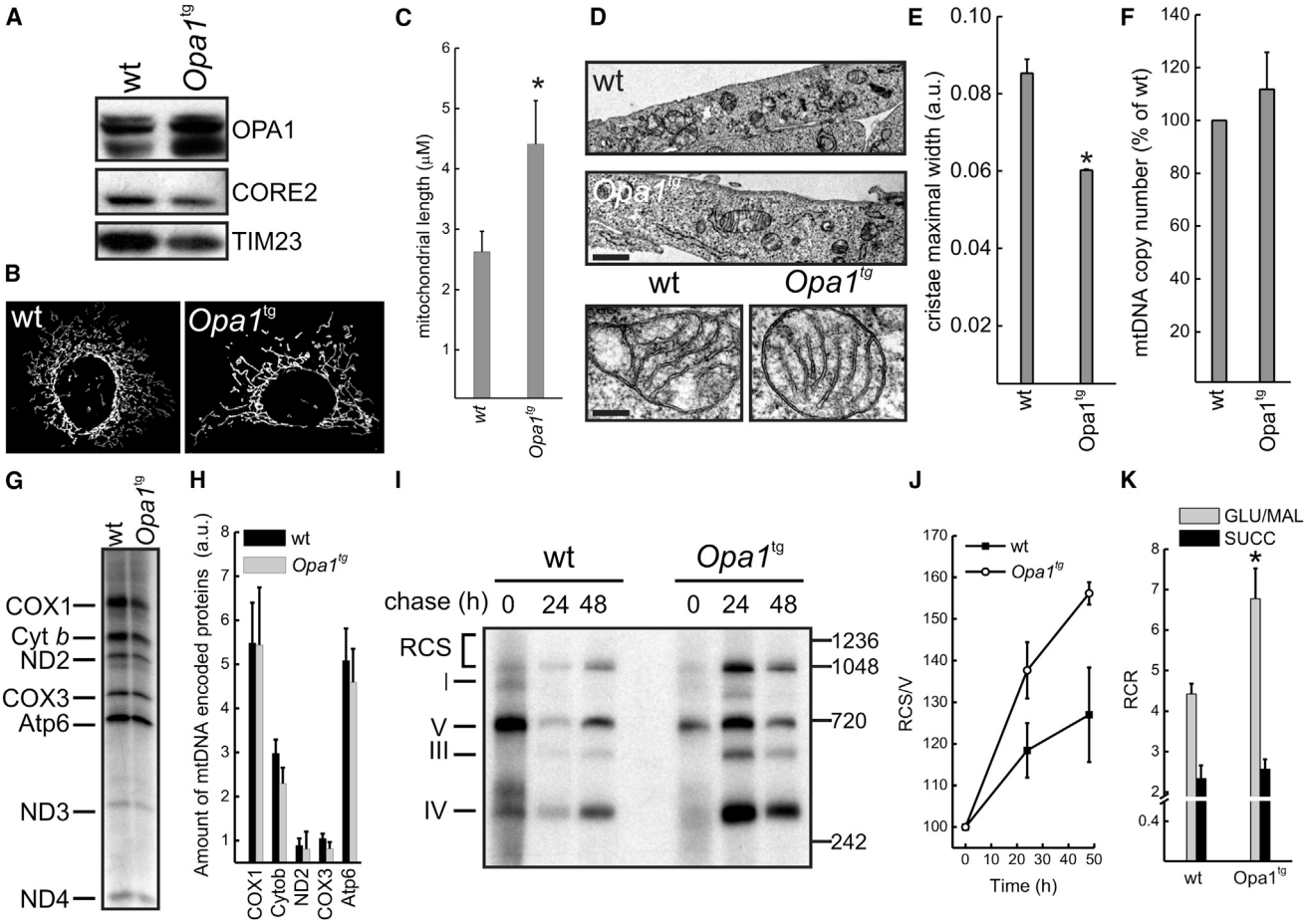

Figure 5. Transgenic Overexpression of OPA1 Increases RCS Assembly

(A) Equal amounts of proteins (20 μg) from MAFs of the indicated genotypes were separated by SDS-PAGE and immunoblotted with the indicated antibodies.

(B) Representative confocal micrographs of mitochondrial morphology in WT and Opa1^{tg} MAFs. Mitochondria were visualized by anti-TOM20 immunostaining. The scale bar represents 20 μM.

(C) Average mitochondrial major axis length. Experiments were as in (B). Data represent average ± SEM of four independent experiments (five mitochondria per cell, at least 50 cells/experiment). The asterisk denotes $p < 0.05$ in a paired sample Student's t test versus WT.

(D) Electron micrographs of MAFs of the indicated genotype. The scale bars represent 2 μm (top) and 200 nm (bottom).

(E) Morphometric analysis of cristae width in 40 randomly selected mitochondria of MAFs of the indicated genotype. Data represent average ± SEM of three independent experiments. The asterisk denotes $p < 0.05$ in a paired sample Student's t test versus WT.

(F) Mitochondrial DNA copy number quantification. mtDNA was amplified by RT-PCR from total DNA of MAFs of the indicated genotype. Data are normalized to WT MAFs and represent the average ± SEM of four independent experiments.

(G) mtDNA translation assay. MAFs of the indicated genotype were metabolic labeled in presence of emetine and lysed after 30 min. Protein samples (40 μg) were separated by SDS-PAGE, and the radioactivity was detected in the fixed and dried gels for 3 days. The mtDNA-encoded proteins are indicated.

(H) Densitometric analysis of the mtDNA-encoded proteins. Experiments are as in (G). Data represent average ± SEM of four independent experiments.

(I) RCS assembly assay. MAFs of the indicated genotype were metabolically labeled for 2 hr and then chased for the indicated times. Equal amounts of protein (100 μg) were separated by BN PAGE, and radioactivity was detected in the fixed and dried gels for 1 week. Individual complexes and supercomplexes of the respiratory chain are indicated.

(J) Densitometric analysis of the incorporation rate of radioactivity into RCS. Values are normalized for the autoradiographic signal of complex V. Data represent average ± SEM of three independent experiments performed as in (H).

(K) RCR of mitochondria isolated from livers of mice of the indicated genotype energized with 5 mM/2.5 mM GLU/MAL or 10 mM SUCC. Data represent mean ± SEM of four independent experiments. The asterisk denotes $p < 0.05$ in a paired sample Student's t test versus WT.

See also Figure S5.

intrinsic apoptosis (Frezza et al., 2006; Yamaguchi et al., 2008; Costa et al., 2010), cristae remodeling has been reckoned as a mere feedback mechanism in situ, occurring after caspase activation (Sun et al., 2007). Our results suggest that, in addition to its role in cytochrome *c* release, cristae remodeling also impairs mitochondrial function to precipitate apoptosis. The BID α6 mutant generated here, which does not induce cristae changes and cytochrome *c* mobilization but permeabilizes the outer

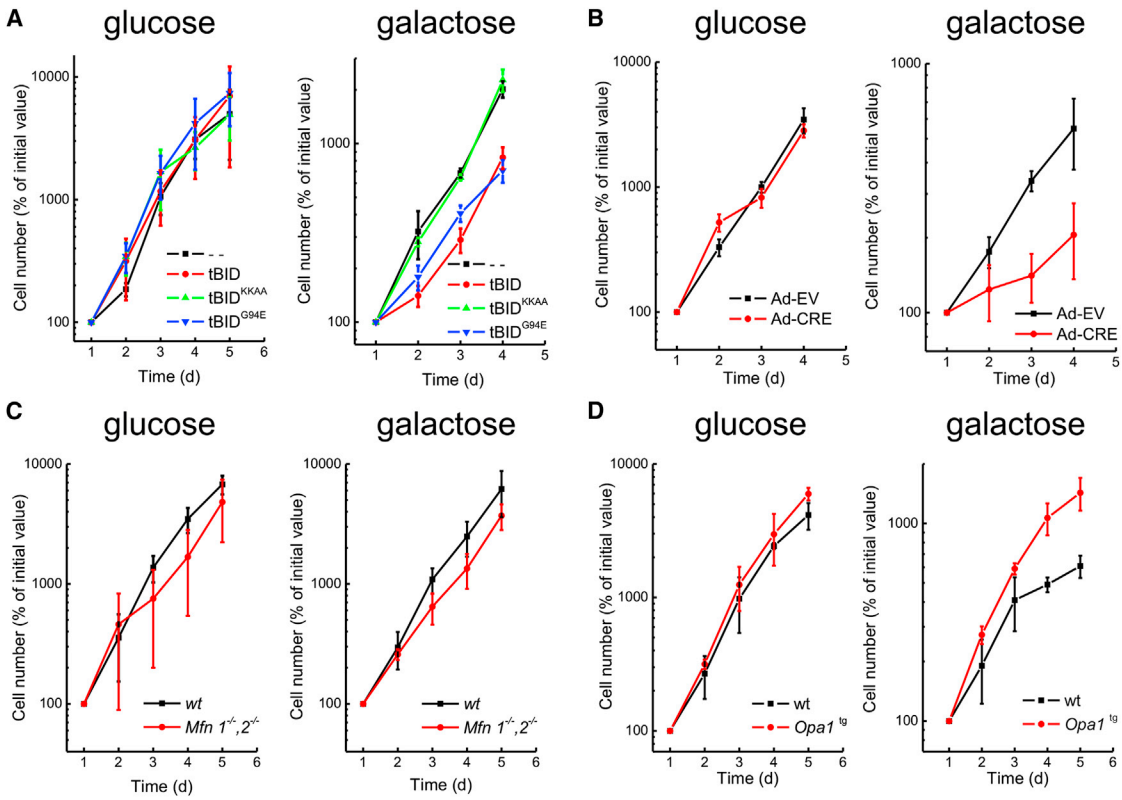

Figure 6. Mitochondria-Dependent Cellular Growth Requires Assembled RCS

(A) Growth curves of DKO MEFs transduced with the indicated retroviruses and grown in DMEM supplemented with the indicated monosaccharides. Data represent mean ± SEM of five independent experiments.

(B–D) Growth curves of the indicated cell lines cultured in DMEM supplemented with the indicated monosaccharides. Data represent mean ± SEM of five independent experiments.

See also Figure S6.

membrane, can be a useful tool to dissect in vivo the involvement of cristae remodeling in developmental and homeostatic apoptosis. We think that cristae remodeling influences RCS by targeting OPA1 (Frezza et al., 2006), not by altering membrane potential that is normal during cristae remodeling (Scorrano et al., 2002) or by inhibiting mtDNA translation and insertion of mtDNA-encoded subunits that similarly appear normal in DKO cell-expressing BID (data not shown).

Our work unravels a role for cristae shape in RCS assembly and stability, mitochondrial respiratory efficiency, and respiratory growth, suggesting that shape of biological membranes can influence membrane protein complexes. Moreover, our data highlight the importance of RCS in respiration by complex I-feeding substrates. Finally, we unveil how OPA1 regulates mitochondrial respiratory efficiency. The pathogenesis of dominant optic atrophy where OPA1 is mutated (Alexander et al., 2000) or of other mitochondrial diseases where OPA1 is degraded (Duvezin-Caubet et al., 2006) could also depend on this unexpected OPA1 function. In these latter settings, stabilization of OPA1 could correct RCS and therefore mitochondrial dysfunction, opening novel therapeutic perspectives for currently intractable diseases.

EXPERIMENTAL PROCEDURES

Generation of *Opa1*$^{flx/flx}$ and *Opa1*^{tg} Mice

To generate *Opa1*$^{flx/flx}$ mice, a mouse Bac clone containing the *Opa1* gene was isolated from the C57BL/6J ES BAC clone library. An 11 kb HpaI DNA restriction fragment containing the 5 kb upstream-exon3 was subcloned in a pUC-8 vector. The OPA1 fragment was excised with EcoRV and XmaI to generate blunt ends and inserted into a pKO4.4a-LoxP cut with XhoI and SalI. A LoxP site was introduced between intron1 and exon2 of *Opa1* and a phosphoglycerate kinase (PGK) promoter-driven neomycin resistance gene, flanked by two FRT sequences and with one LoxP sequence downstream, was inserted in intron3. The targeting vector was linearized and electroporated into C57BL6 embryonic stem cells (ESCs). Neomycin-resistant ESC clones were tested for homologous recombination. Three mutated ESC lines were microinjected into C57BL6 blastocytes and implanted in host mice to obtain chimeric mice, which were then bred with C57BL6 mates and their offspring tested by PCR for germline transmission. Colonies were established in a C57BL6 background.

To generate *Opa1*^{tg} mice, the human β-actin promoter was extracted from pDRIVE-hβ-ACTIN (InvivoGen) using SpeI and NcoI and cloned in pENTRY. The complementary DNA of mouse isoform 1 *Opa1* and polyA extracted from pcDNA3.1-OPA1 (Cipolat et al., 2004) using Nhe1 and EciI was ligated into pENTRY using Quick Ligase (Ozyme). The transgene was then inserted by homologous recombination in a pDEST vector containing part of the human hypoxanthine phosphoribosyltransferase locus. The resulting vector was

linearized using PvuI and electroporated into C57BL6 BPES cells by Nucleis (France). Homologous recombinants were selected on stringent hypoxanthine aminopterin-thymidine-supplemented medium. Three positive ESC recombinant clones were microinjected into C57BL6 blastocysts and implanted into host pseudopregnant female C57BL6 to obtain chimeric mice. Six chimeras (identified by fur agouti color) were bred with C57BL6 mates, and germline transmission was verified by fur color and PCR. Colonies were established in a C57BL6 and in a Sv129 background by crossbreeding. Details on mouse genotyping and handling can be found in the Extended Experimental Procedures.

BNGE, 2D BN/BNGE, and 2D BN/SDS PAGE

Mitochondria (10 mg/ml) were suspended in buffer D (1 M 6-aminohexanoic acid, 1.25% V/V digitonin, 50 mM Bis-Tris-HCl, pH 7) and centrifuged. The supernatant was collected, and 5% Serva Blue G dye in 1 M 6-aminohexanoic acid was added to 1/3 of the final sample volume. Equal amounts (100 μg) of mitochondrial proteins were separated by 3%–13% gradient BNGE (Schägger, 1995). For RCS detection, the concentration of digitonin in buffer D was 4% (V/V).

For two-dimensional (2D) Blue Native (BN)/BNGE, the lane cut from the first-dimension BNGE was casted on top of a native 3%–14% gradient gel in 1% (V/V) dodecyl maltoside. For 2D BN/SDS PAGE, the lane cut from the first-dimension BNGE was incubated for 1 hr at 25°C in 1% SDS and 1% β-mercaptoethanol and then casted on top of an 8% or a 16.5% denaturing gel. After electrophoresis, the complexes were electroblotted on a polyvinylidene fluoride (PVDF) membrane and probed with the indicated antibodies.

To detect RCS from radiolabelled cells, samples were treated as described above, and after electrophoresis, the gels were dried and the signal was detected following exposure for 3–6 days.

Pulse-Chase Experiments

Labeling of mtDNA-encoded proteins was performed with [^{35}S]-methionine and cysteine (EXPRE^{35}S^{35}S Protein Labeling Mix, Perkin Elmer Life Sciences). Cells were preincubated for 12 hr in the presence of 40 μg/ml chloramphenicol in uridine-supplemented medium and then exposed for 2 hr to the [^{35}S] protein labeling mix (pulse) in the presence of 50 μg/ml cycloheximide. Cells were washed for four times with PBS and cold Dulbecco's modified Eagle's medium (DMEM) and then cultured for the indicated time (chase) prior to lysis and protein separation by BNGE.

To assay basal mtDNA translation, equal protein amounts (40 μg) from cells metabolically labeled as described above treated for 30 min with 50 μg/ml emetine were separated by SDS-PAGE.

Mitochondrial Assays

Mitochondria from liver of mice and from the indicated cell lines were isolated as in Frezza et al. (2007). Cytochrome *c* release, ascorbate/TMPD-driven respiration and cytochrome b_5-dependent NADH oxidation were determined as described (Scorrano et al., 2002). Details can be found in the Extended Experimental Procedures.

Biochemistry

For protein crosslinking, mitochondria treated as indicated were incubated with 1 mM 1-ethyl-3-[3-dimethylaminopropyl]carbodiimide hydrochloride (EDC) or 1 mM bismaleimidohexane (BMH), as previously described (Frezza et al., 2006). Carbonate extraction was performed as previously described (Dimmer et al., 2008). Details and procedures for SDS-PAGE and immunoblotting can be found in the Extended Experimental Procedures.

Molecular Biology

The retroviral vector pMIG-tBid was described previously (Cheng et al., 2001). KKAA, G94E, and G94EKKAA mutants were generated by site-direct mutagenesis using KOD polymerase (Biolabs). Details can be found in the Extended Experimental Procedures.

To measure mtDNA copy number, total cellular DNA was amplified using specific oligodeoxynucleotides for *mt-Co2* and *Sdha* by real-time PCR. Details can be found in the Extended Experimental Procedures.

Cell Biology

MEFs and human embryonic kidney 293 cells (HEK293) cells were cultured as described (Gomes et al., 2011). When indicated, in DMEM, glucose was substituted with 0.9 mg/ml galactose. Ecotropic viruses were generated as described (Cheng et al., 2001). WT, *Opa1*$^{flx/flx}$, *Opa1*^{tg}, and MAFs SV40 transformed cell lines were generated from the diaphragm of the respective 7-week-old mouse killed by cervical dislocation. Details on the procedure can be found in the Extended Experimental Procedures. Acute *Opa1* ablation in *Opa1*$^{flx/flx}$ MAFs was obtained by infection with adenoviruses expressing cytomegalovirus (CMV)-Cre-GFP (ad-CRE; 300 pfu/cell; Vector Biolabs). CMV-GFP (ad-EV)-expressing adenoviruses were used as control.

Cell growth was determined by counting viable cells for the indicated time. *Opa1*$^{flx/flx}$ MAFs were infected and DKO MEFs were transduced 24 or 16 hr before the growth was assessed.

Apoptosis was measured by flow cytometric detection (FACSCalibur) of the Annexin-V-PE positive events in the GFP-positive population. Details can be found in the Extended Experimental Procedures.

Imaging and Transmission Electron Microscopy

For mitochondrial imaging, cells stained with a rabbit polyclonal anti-TOM20 (Santa Cruz; 1:200), as previously described (Frezza et al., 2006), were analyzed by confocal microscopy. Adenovirus-infected cells were identified by GFP expression. Electron microscopy (EM) was performed as described (Scorrano et al., 2002). Details can be found in the Extended Experimental Procedures.

SUPPLEMENTAL INFORMATION

Supplemental Information includes Extended Experimental Procedures and six figures and can be found with this article online at http://dx.doi.org/10.1016/j.cell.2013.08.032.

ACKNOWLEDGMENTS

We thank A. Gross (Weizmann Institute) for anti-BID antibody, A. Latorre-Pellicer (CNIC) for mtDNA RT-PCR, and M. Albiero (VIMM) for tail vein injections. L.S. is a senior scientist of the Dulbecco-Telethon Institute. This work is supported by Telethon Italy (GGP12162, GPP10005B, and TCR02016), AIRC Italy, MOH Italy (GR 09.021), and Swiss National Foundation (31-118171). J.A.E. is supported by MINECO (SAF2012-32776 and CSD2007-00020), DGA (B55, PIPAMER O905), and CAM (S2011/BMD-2402). S.C. was supported by a Journal of Cell Science Travelling Fellowship. C.F. was supported by an AIRC Biennial Fellowship. The CNIC is funded by the Instituto de Salud Carlos III-MICINN and the Pro-CNIC Foundation.

Received: December 28, 2012
Revised: July 25, 2013
Accepted: August 19, 2013
Published: September 19, 2013

REFERENCES

Acín-Pérez, R., Bayona-Bafaluy, M.P., Fernández-Silva, P., Moreno-Loshuertos, R., Pérez-Martos, A., Bruno, C., Moraes, C.T., and Enríquez, J.A. (2004). Respiratory complex III is required to maintain complex I in mammalian mitochondria. Mol. Cell *13*, 805–815.

Acín-Pérez, R., Fernández-Silva, P., Peleato, M.L., Pérez-Martos, A., and Enriquez, J.A. (2008). Respiratory active mitochondrial supercomplexes. Mol. Cell *32*, 529–539.

Alexander, C., Votruba, M., Pesch, U.E., Thiselton, D.L., Mayer, S., Moore, A., Rodriguez, M., Kellner, U., Leo-Kottler, B., Auburger, G., et al. (2000). OPA1, encoding a dynamin-related GTPase, is mutated in autosomal dominant optic atrophy linked to chromosome 3q28. Nat. Genet. *26*, 211–215.

Campanella, M., Casswell, E., Chong, S., Farah, Z., Wieckowski, M.R., Abramov, A.Y., Tinker, A., and Duchen, M.R. (2008). Regulation of mitochondrial

structure and function by the F1Fo-ATPase inhibitor protein, IF1. Cell Metab. *8*, 13–25.

Cereghetti, G.M., Stangherlin, A., Martins de Brito, O., Chang, C.R., Blackstone, C., Bernardi, P., and Scorrano, L. (2008). Dephosphorylation by calcineurin regulates translocation of Drp1 to mitochondria. Proc. Natl. Acad. Sci. USA *105*, 15803–15808.

Chen, H., Detmer, S.A., Ewald, A.J., Griffin, E.E., Fraser, S.E., and Chan, D.C. (2003). Mitofusins Mfn1 and Mfn2 coordinately regulate mitochondrial fusion and are essential for embryonic development. J. Cell Biol. *160*, 189–200.

Chen, H., Vermulst, M., Wang, Y.E., Chomyn, A., Prolla, T.A., McCaffery, J.M., and Chan, D.C. (2010). Mitochondrial fusion is required for mtDNA stability in skeletal muscle and tolerance of mtDNA mutations. Cell *141*, 280–289.

Chen, Y.C., Taylor, E.B., Dephoure, N., Heo, J.M., Tonhato, A., Papandreou, I., Nath, N., Denko, N.C., Gygi, S.P., and Rutter, J. (2012). Identification of a protein mediating respiratory supercomplex stability. Cell Metab. *15*, 348–360.

Cheng, E.H., Wei, M.C., Weiler, S., Flavell, R.A., Mak, T.W., Lindsten, T., and Korsmeyer, S.J. (2001). BCL-2, BCL-X(L) sequester BH3 domain-only molecules preventing BAX- and BAK-mediated mitochondrial apoptosis. Mol. Cell *8*, 705–711.

Cipolat, S., Martins de Brito, O., Dal Zilio, B., and Scorrano, L. (2004). OPA1 requires mitofusin 1 to promote mitochondrial fusion. Proc. Natl. Acad. Sci. USA *101*, 15927–15932.

Cipolat, S., Rudka, T., Hartmann, D., Costa, V., Serneels, L., Craessaerts, K., Metzger, K., Frezza, C., Annaert, W., D'Adamio, L., et al. (2006). Mitochondrial rhomboid PARL regulates cytochrome c release during apoptosis via OPA1-dependent cristae remodeling. Cell *126*, 163–175.

Costa, V., Giacomello, M., Hudec, R., Lopreiato, R., Ermak, G., Lim, D., Malorni, W., Davies, K.J., Carafoli, E., and Scorrano, L. (2010). Mitochondrial fission and cristae disruption increase the response of cell models of Huntington's disease to apoptotic stimuli. EMBO Mol Med *2*, 490–503.

Danial, N.N., and Korsmeyer, S.J. (2004). Cell death: critical control points. Cell *116*, 205–219.

Davies, K.M., Strauss, M., Daum, B., Kief, J.H., Osiewacz, H.D., Rycovska, A., Zickermann, V., and Kühlbrandt, W. (2011). Macromolecular organization of ATP synthase and complex I in whole mitochondria. Proc. Natl. Acad. Sci. USA *108*, 14121–14126.

de Brito, O.M., and Scorrano, L. (2008). Mitofusin 2 tethers endoplasmic reticulum to mitochondria. Nature *456*, 605–610.

Dimmer, K.S., and Scorrano, L. (2006). (De)constructing mitochondria: what for? Physiology (Bethesda) *21*, 233–241.

Duvezin-Caubet, S., Jagasia, R., Wagener, J., Hofmann, S., Trifunovic, A., Hansson, A., Chomyn, A., Bauer, M.F., Attardi, G., Larsson, N.G., et al. (2006). Proteolytic processing of OPA1 links mitochondrial dysfunction to alterations in mitochondrial morphology. J. Biol. Chem. *281*, 37972–37979.

Frey, T.G., and Mannella, C.A. (2000). The internal structure of mitochondria. Trends Biochem. Sci. *25*, 319–324.

Frezza, C., Cipolat, S., Martins de Brito, O., Micaroni, M., Beznoussenko, G.V., Rudka, T., Bartoli, D., Polishuck, R.S., Danial, N.N., De Strooper, B., and Scorrano, L. (2006). OPA1 controls apoptotic cristae remodeling independently from mitochondrial fusion. Cell *126*, 177–189.

Germain, M., Mathai, J.P., McBride, H.M., and Shore, G.C. (2005). Endoplasmic reticulum BIK initiates DRP1-regulated remodelling of mitochondrial cristae during apoptosis. EMBO J. *24*, 1546–1556.

Gomes, L.C., Di Benedetto, G., and Scorrano, L. (2011). During autophagy mitochondria elongate, are spared from degradation and sustain cell viability. Nat. Cell Biol. *13*, 589–598.

Green, D.R., and Kroemer, G. (2004). The pathophysiology of mitochondrial cell death. Science *305*, 626–629.

Griparic, L., and van der Bliek, A.M. (2001). The many shapes of mitochondrial membranes. Traffic *2*, 235–244.

Hackenbrock, C.R. (1966). Ultrastructural bases for metabolically linked mechanical activity in mitochondria. I. Reversible ultrastructural changes with change in metabolic steady state in isolated liver mitochondria. J. Cell Biol. *30*, 269–297.

Landes, T., Emorine, L.J., Courilleau, D., Rojo, M., Belenguer, P., and Arnauné-Pelloquin, L. (2010). The BH3-only Bnip3 binds to the dynamin Opa1 to promote mitochondrial fragmentation and apoptosis by distinct mechanisms. EMBO Rep. *11*, 459–465.

Lapuente-Brun, E., Moreno-Loshuertos, R., Acín-Pérez, R., Latorre-Pellicer, A., Colás, C., Balsa, E., Perales-Clemente, E., Quirós, P.M., Calvo, E., Rodríguez-Hernández, M.A., et al. (2013). Supercomplex assembly determines electron flux in the mitochondrial electron transport chain. Science *340*, 1567–1570.

Legros, F., Lombès, A., Frachon, P., and Rojo, M. (2002). Mitochondrial fusion in human cells is efficient, requires the inner membrane potential, and is mediated by mitofusins. Mol. Biol. Cell *13*, 4343–4354.

Lodi, R., Tonon, C., Valentino, M.L., Iotti, S., Clementi, V., Malucelli, E., Barboni, P., Longanesi, L., Schimpf, S., Wissinger, B., et al. (2004). Deficit of in vivo mitochondrial ATP production in OPA1-related dominant optic atrophy. Ann. Neurol. *56*, 719–723.

Merkwirth, C., Dargazanli, S., Tatsuta, T., Geimer, S., Löwer, B., Wunderlich, F.T., von Kleist-Retzow, J.C., Waisman, A., Westermann, B., and Langer, T. (2008). Prohibitins control cell proliferation and apoptosis by regulating OPA1-dependent cristae morphogenesis in mitochondria. Genes Dev. *22*, 476–488.

Minauro-Sanmiguel, F., Wilkens, S., and García, J.J. (2005). Structure of dimeric mitochondrial ATP synthase: novel F0 bridging features and the structural basis of mitochondrial cristae biogenesis. Proc. Natl. Acad. Sci. USA *102*, 12356–12358.

Paumard, P., Vaillier, J., Coulary, B., Schaeffer, J., Soubannier, V., Mueller, D.M., Brèthes, D., di Rago, J.P., and Velours, J. (2002). The ATP synthase is involved in generating mitochondrial cristae morphology. EMBO J. *21*, 221–230.

Pfeiffer, D.R., Gudz, T.I., Novgorodov, S.A., and Erdahl, W.L. (1995). The peptide mastoparan is a potent facilitator of the mitochondrial permeability transition. J. Biol. Chem. *270*, 4923–4932.

Santel, A., and Fuller, M.T. (2001). Control of mitochondrial morphology by a human mitofusin. J. Cell Sci. *114*, 867–874.

Santel, A., Frank, S., Gaume, B., Herrler, M., Youle, R.J., and Fuller, M.T. (2003). Mitofusin-1 protein is a generally expressed mediator of mitochondrial fusion in mammalian cells. J. Cell Sci. *116*, 2763–2774.

Schägger, H. (1995). Native electrophoresis for isolation of mitochondrial oxidative phosphorylation protein complexes. Methods Enzymol. *260*, 190–202.

Scorrano, L., Ashiya, M., Buttle, K., Weiler, S., Oakes, S.A., Mannella, C.A., and Korsmeyer, S.J. (2002). A distinct pathway remodels mitochondrial cristae and mobilizes cytochrome c during apoptosis. Dev. Cell *2*, 55–67.

Smirnova, E., Griparic, L., Shurland, D.L., and van der Bliek, A.M. (2001). Dynamin-related protein Drp1 is required for mitochondrial division in mammalian cells. Mol. Biol. Cell *12*, 2245–2256.

Strauss, M., Hofhaus, G., Schröder, R.R., and Kühlbrandt, W. (2008). Dimer ribbons of ATP synthase shape the inner mitochondrial membrane. EMBO J. *27*, 1154–1160.

Strogolova, V., Furness, A., Robb-McGrath, M., Garlich, J., and Stuart, R.A. (2012). Rcf1 and Rcf2, members of the hypoxia-induced gene 1 protein family, are critical components of the mitochondrial cytochrome bc1-cytochrome c oxidase supercomplex. Mol. Cell. Biol. *32*, 1363–1373.

Sun, M.G., Williams, J., Munoz-Pinedo, C., Perkins, G.A., Brown, J.M., Ellisman, M.H., Green, D.R., and Frey, T.G. (2007). Correlated three-dimensional light and electron microscopy reveals transformation of mitochondria during apoptosis. Nat. Cell Biol. *9*, 1057–1065.

Vogel, F., Bornhövd, C., Neupert, W., and Reichert, A.S. (2006). Dynamic subcompartmentalization of the mitochondrial inner membrane. J. Cell Biol. *175*, 237–247.

Vukotic, M., Oeljeklaus, S., Wiese, S., Vögtle, F.N., Meisinger, C., Meyer, H.E., Zieseniss, A., Katschinski, D.M., Jans, D.C., Jakobs, S., et al. (2012). Rcf1 mediates cytochrome oxidase assembly and respirasome formation, revealing heterogeneity of the enzyme complex. Cell Metab. *15*, 336–347.

Wei, M.C., Lindsten, T., Mootha, V.K., Weiler, S., Gross, A., Ashiya, M., Thompson, C.B., and Korsmeyer, S.J. (2000). tBID, a membrane-targeted death ligand, oligomerizes BAK to release cytochrome c. Genes Dev. *14*, 2060–2071.

Wei, M.C., Zong, W.X., Cheng, E.H., Lindsten, T., Panoutsakopoulou, V., Ross, A.J., Roth, K.A., MacGregor, G.R., Thompson, C.B., and Korsmeyer, S.J. (2001). Proapoptotic BAX and BAK: a requisite gateway to mitochondrial dysfunction and death. Science *292*, 727–730.

Yamaguchi, R., Lartigue, L., Perkins, G., Scott, R.T., Dixit, A., Kushnareva, Y., Kuwana, T., Ellisman, M.H., and Newmeyer, D.D. (2008). Opa1-mediated cristae opening is Bax/Bak and BH3 dependent, required for apoptosis, and independent of Bak oligomerization. Mol. Cell *31*, 557–569.

Yoon, Y., Pitts, K.R., and McNiven, M.A. (2001). Mammalian dynamin-like protein DLP1 tubulates membranes. Mol. Biol. Cell *12*, 2894–2905.

Zanna, C., Ghelli, A., Porcelli, A.M., Karbowski, M., Youle, R.J., Schimpf, S., Wissinger, B., Pinti, M., Cossarizza, A., Vidoni, S., et al. (2008). OPA1 mutations associated with dominant optic atrophy impair oxidative phosphorylation and mitochondrial fusion. Brain *131*, 352–367.

Cell

EXTENDED EXPERIMENTAL PROCEDURES

Mouse Handling

For genotyping of the *Opa1*$^{flx/flx}$ mice, the following primers were used: PRIMER Ck1 5′-CAG TGT TGA TGA CAG CTC AG-3′; PRIMER Ck2 5′-CAT CAC ACA CTA GCT TAC ATT TGC-3′. For genotyping of the *Opa1*^{tg} mice, the following primers were used: PRIMER tgF 5′-GCA ATG ACG TGG TCC TGT TTTG-3′; PRIMER tgR 5′-GAT AGG TCA GGT AAG CAA GCA AC-3′; PRIMER wtR 5′-GAG GGA GAA AAA TGC GGA GTG-3′; PRIMER wtF 5′-CTC CGG AAA GCA GTG AGG TAA G-3′.

All mice procedures were performed according to protocols approved by the local Ethic committees (protocol 32/2011 CEASA University of Padova, Venetian Institute of Molecular Medicine; license 1034/3703/02 Cantonal Veterinarian Authority, University of Geneva). *Opa1*$^{flx/flx}$ mice were tail injected with adenoviruses (2x10^9 Pfu) (Vector Biolabs). After 3 days, they were killed by cervical dislocation and the liver was extracted.

Mitochondrial Assays

Mitochondria from mouse liver and from the indicated cell lines were isolated as described (Frezza et al., 2007). Mitochondria were isolated from *Opa1*$^{flx/flx}$ mice 3 days after the tail-vein injection of the indicated adenoviruses. Cytochrome *c* release, ascorbate/TMPD-driven respiration and Cytochrome b_5-dependent NADH oxidation were determined as described (Scorrano et al., 2002). To measure respiration, mitochondria (1 mg/ml) were incubated in Experimental Buffer (EB: 150 mM KCl, 10 mM Tris Mops, 10 μM EGTA-Tris, 10μM ATP). To determine BID effect of RCR, EB was supplemented with 5 μM cytochrome *c*, 2 mM NADH and 3.2 pmol × mg^{-1} cBID. When indicated, mitochondria were transferred into a Clark's type oxygen electrode chamber and 5 mM glutamate /2.5 mM malate or 2 μM rotenone/10 mM succinate were added. Basal O_2 consumption was recorded (state 2) and after 2 min 100 μM ADP was added (state 3), followed by 2.5 μg/ml oligomycin (state 4) and 200 μM FCCP (state 3u). For complex IV dependent-O_2 consumption, mitochondria (1 mg/ml) were incubated for the indicated time in EB supplemented with 5 μM cytochrome *c*. Mitochondria were treated with 1 nmol/mg Antimycin A and 2 nM rotenone and they were transferred into a Clark's type oxygen electrode chamber. After 2 min 6 mM Ascorbate and 300 μM TMPD were added and the Complex IV-dependent O_2 consumption rate was measured.

The enzymatic activity of Complex I and citrate synthase was determined as described (Spinazzi et al., 2012).

Transmission Electron Microscopy

EM of cells and isolated mitochondria were performed as described (Scorrano et al., 2002) and thin sections were imaged on a Tecnai-20 electron microscope (Philips-FEI). For morphometric analysis of mitochondrial cristae, cristae width was measured using the Image J Multimeasure plug-in.

Measurement of Mitochondrial DNA Copy Number

Total cellular DNA was isolated using phenol/chlorophorm 24:25 (v/v) and was amplified using specific oligodeoxynucleotides for *mt-Co2* and *Sdha* by real-time PCR using Platinum SYBR Green qPCR Supermix (Invitrogen) following manufacturer's indications. The mtDNA copy number per cell was calculated using *Sdha* amplification as a reference for nuclear DNA content.

Imaging

4x10^3 cells seeded on 13 mm round glass coverslips were fixed, permeabilized and blocked as previously described (Frezza et al., 2006) and then stained with a rabbit polyclonal anti-TOM20 (Santa Cruz, 1:200) overnight at 4°C. After washing with PBS, cells were incubated with TexasRed conjugated goat anti-rabbit (1:500, Invitrogen) for 1 hr at room temperature and coverslips were mounted on slides using ProLong Gold antifade reagent (Invitrogen) and analyzed by confocal microscopy. Adenovirus infected cells were identified by expression of GFP.

Confocal images were acquired using a Nikon Eclipse TE300 inverted microscope equipped with a spinning-disk PerkinElmer Ultraview LCI confocal system, a piezoelectric z axis motorized stage (Pifoc, Physik Instrumente), and an Orca ER 12-bit CCD camera (Hamamatsu Photonics). For detection of GFP or TexasRed fluorescence, samples were excited using the 488 nm or the 543 nm lines of a He–Ne laser (PerkinElmer, Waltham, MA, USA) with exposure times of 100-200 ms using a 60X, 1.4 NA Plan Apo objective (Nikon). Measurement of mitochondrial major axis length was performed in at least five mitochondria per cell, in a minimum of 50 cells/experiment (250 mitochondria/experiment). Mitochondrial length was then quantified using the ROI Manager plug-in of ImageJ software.

Biochemistry

For protein crosslinking, mitochondria treated as indicated were incubated with 1 mM EDC or 1 mM BMH as previously described (Frezza et al., 2006). For SDS-PAGE, mitochondrial proteins (20 μg) were separated on 3%–8% Tris-acetate or 4%–12% Tris-glycine (NuPage, Invitrogen) polyacrilamide gels, transferred onto PVDF membranes (Biorad) and probed using the indicated primary antibodies and isotype matched secondary antibodies conjugated to horseradish peroxidase whose signal was detected with ECL (Amersham). The following primary antibodies were employed: Monoclonal anti-OPA1 (1:1000 BD PharMingen), rabbit polyclonal anti-BAK-NT (1:1000 Upstate), mouse monoclonal anti-Fp subunit (1:5000), mouse monoclonal anti-NDUFA9 subunit (1:1000),

mouse monoclonal anti-Core2 subunit (1:1000), mouse monoclonal anti-CO1subunit (1:1000) (MitoScience), mouse monoclonal anti-VDAC1 (1:1000 Abcam), rabbit polyclonal anti-TOM20 (1:1000 Santa Cruz), mouse monoclonal anti-TIM23 (1:1000 BD PharMingen), rabbit polyclonal anti-BID (1:1,000, a kind gift of A. Gross, Weizmann Institute, Rehovot). Densitometry was performed by analyzing optical density using Gel Pro Analyzer.

Carbonate extraction was performed as previously described (Dimmer et al., 2008).

Molecular Biology

The retroviral vector pMIG-tBid was described previously (Cheng et al., 2001). KKAA, G94E and G94EKKAA mutants were generated by site-direct mutagenesis using KOD polymerase (Biolabs) and the following primers: for BID^{KKAA} forward 5′-ACA ATG CTG TTG GCC GCC GCC GTG GCC AGT CAC-3′ and reverse 5′-GTG ACT GGC CAC GGC GGC GGC CAA CAG CAT TGT-3′; for BID^{G94E} forward 5′-CTC GCC CAA ATA GAA GAT GAG ATG GAC CAC AAC-3′ and reverse 5′-GTT GTG GTC CAT CTC ATC TTC TAT TTG GGC GAG-3′.

Recombinant Protein Expression

p7/p15 recombinant BID was produced, purified and cleaved with caspase-8 as described (Frezza et al., 2006).

Assays of Cell Growth and Death

The growth of WT, *Opa1*^{tg} MAFs was determined by counting viable cells (as determined by Trypan Blue exclusion) daily for 5 days. $1.5x10^4$ *Opa1*$^{flx/flx}$ MAFs were infected with the indicated adenoviruses and after 24 hr the growth was determined by counting viable cells (as determined by Trypan Blue exclusion) daily for 4 days. $1.5x10^4$ DKO MEFs were transduced with the indicated retroviruses and after 16 hr the growth was determined by counting viable GFP positive cells by flow cytometry.

For measurements of apoptosis, $1.5x10^5$ cells of the indicated genotype grown in 6 well-plates were transfected with the indicated vector. After 48 hr apoptosis was measured by flow cytometric detection (FACSCalibur) of the Annexin-V-PE positive events in the GFP-positive population.

Cell Culture, Transfection, Virus Production, and Transduction

DKO MEFs and HEK293 cells were cultured as previously described (Gomes et al., 2011). When indicated, glucose in DMEM was substituted with 0.9 mg/ml galactose. Cells were transfected using Transfectin (Biorad) following manufacturer's instruction.

Ecotropic viruses were generated by cotransfecting the HEK293 packaging cell lines with the packaging vector pIK and the appropriate pMIG as previously described (Cheng et al., 2001). Viral supernatant were retrieved and used to transduce DKO MEFs in the presence of 4 μg/ml of Hexadimethrine Bromide (Sigma). Following an over-night transduction, the rate of GFP expression was typically around 70% as determined by flow cytometry.

WT, *Opa1*$^{flx/flx}$, *Opa1*^{tg}, MAFs SV40 transformed cell lines were generated respectively from WT, *Opa1*$^{flx/flx}$, *Opa1*^{tg} mice. Male 7 weeks old mice were killed by cervical dislocation and their diaphragm were carefully dissected, washed in DMEM, minced and then enzymatically digested with a collagenase 0.5% (Sigma) solution for 10 min at 37°C. The reaction was stopped by adding DMEM supplemented with 10% FBS. Cell were spun at 200 g for 3 min, resuspended in DMEM containing 4.5 mg/ml glucose, 10% fetal bovine serum (FBS), 50 U/ml Penicillin, 50 μg/ml Streptomycin, 100 μM nonessential aminoacids (GIBCO), 50 μg/ml Uridine, 25 mM HEPES (GIBCO), 2.5 μg/ml Fungizone (GIBCO) and seeded on a 0.1% gelatin (Sigma) precoated plate. After 15 min the supernatant was removed and the adherent fibroblasts were left growing in complete DMEM. MAFs were transformed using an SV40 large T antigen expressing plasmid as previously described (Cipolat et al., 2006) and the transformed cells were enriched by serial limiting dilution.

SUPPLEMENTAL REFERENCES

Dimmer, K.S., Navoni, F., Casarin, A., Trevisson, E., Endele, S., Winterpacht, A., Salviati, L., and Scorrano, L. (2008). LETM1, deleted in Wolf-Hirschhorn syndrome is required for normal mitochondrial morphology and cellular viability. Hum. Mol. Genet. *17*, 201–214.

Frezza, C., Cipolat, S., and Scorrano, L. (2007). Organelle isolation: functional mitochondria from mouse liver, muscle and cultured fibroblasts. Nat. Protoc. *2*, 287–295.

Spinazzi, M., Casarin, A., Pertegato, V., Salviati, L., and Angelini, C. (2012). Assessment of mitochondrial respiratory chain enzymatic activities on tissues and cultured cells. Nat. Protoc. *7*, 1235–1246.

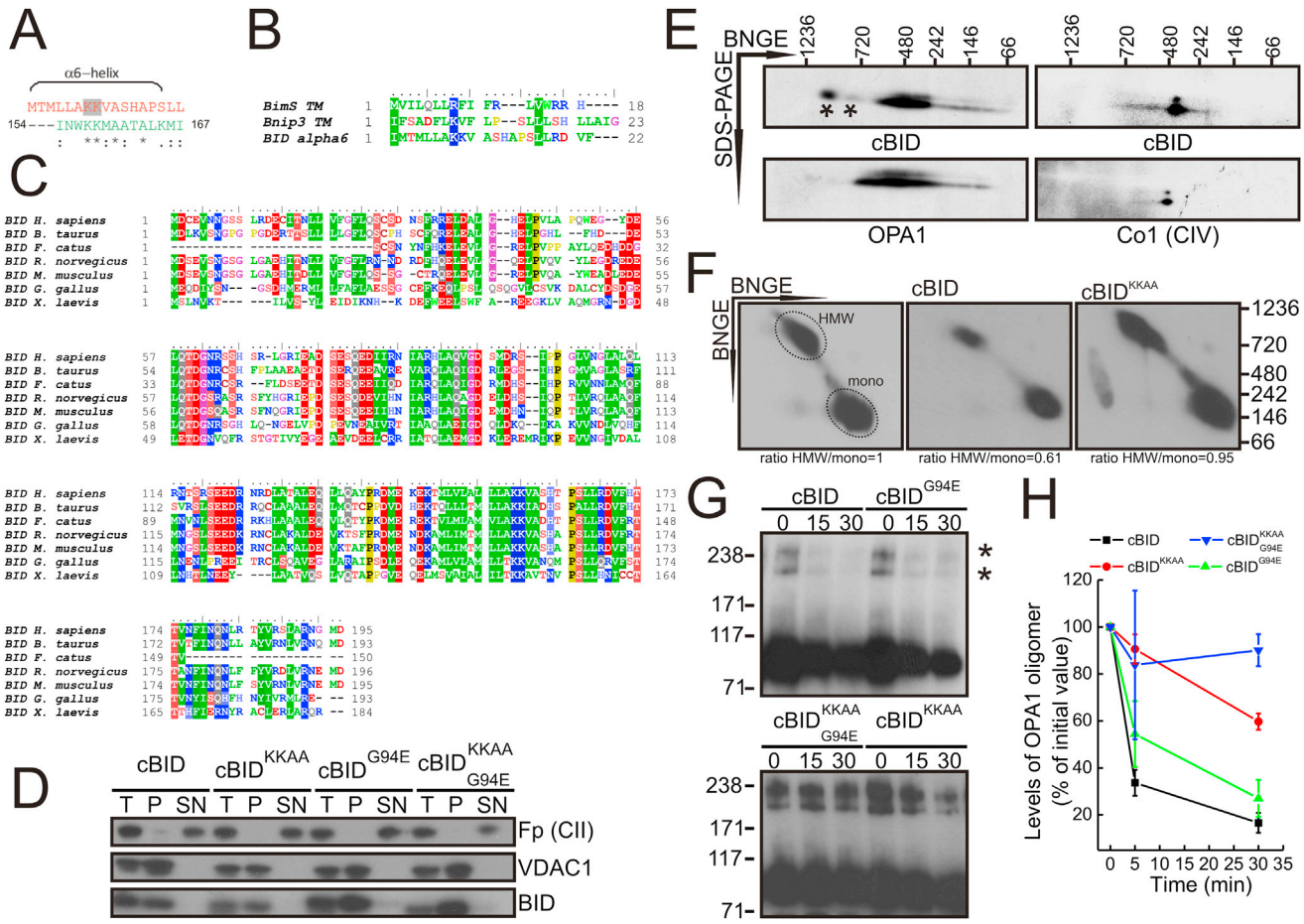

Figure S1. The Conserved BID α6 Helix K157, K158 Residues Are Required to Destabilize OPA1 HMW Complexes, Related to Figure 1

(A) ClustalW alignment between the amino acid sequence of the BID hydrophobic α-6helix of BID (red) and Mastoparan (green). Asterisk: identical aa.; colon: high homology; dot: homology. Two conserved Lysine residues (K157, 158) are highlighted in gray.

(B) ClustalW alignment between the amino acidic sequence of the transmembrane domain of BimS and Bnip3 and the α6-helix of BID.

(C) ClustalW alignment of the amino acidic sequence of BID of different species. Identical aa. are indicated in the same color.

(D) Mouse liver mitochondria were treated with the indicated mutants of cBID for 30 min and peripheral proteins were extracted by incubation in 0.1 M Na_2CO_3 pH 11.3, for 30 min. Membrane and soluble fractions were recovered after centrifugation. Equal amount of proteins (10 μg) were separated by SDS-PAGE and immunoblotted with the indicated antibodies (T: total lysate, P: pellet, SN: supernatant).

(E) 2D BN/SDS-PAGE analysis of the OPA1 oligomers and complex IV. Mitochondria were treated as indicated for 30 min. Equal amount (50 μg) of proteins were separated in native condition and then the lanes were excised and proteins separated by a second dimension SDS-PAGE. After immunoblotting, the proteins were immunodecorated with the indicated antibody. Asterisk indicates high molecular weight complexes of OPA1.

(F) 2D BN/BN-PAGE analysis of OPA1 oligomers in mitochondria treated as indicated for 30 min. Equal amounts (50 μg) of proteins were separated in native condition and then the lane was cut and proteins were separated by a second dimension native page. The complexes were immunoblotted and probed with anti-OPA1 antibody. The circled areas were used for densitometry and the ratio between the HMW and the monomeric (mono) OPA1 forms are reported below each panel. For the sake of clarity, the ratio in untreated mitochondria has been set to 1 and the values in cBID treated mitochondria normalized to the untreated one.

(G) Mitochondria treated with the indicated mutants of cBID for the indicated minutes were crosslinked with 1 mM EDC for 30 min, and equal amount (20 μg) of proteins in the pellet were separated by SDS-PAGE and immunoblotted with anti-OPA1 antibody. Asterisks indicate OPA1 oligomers.

(H) Kinetics of OPA1 oligomers destabilization by cBID. Experiments were as in (C). Data represent average ± SEM of 5 independent experiments.

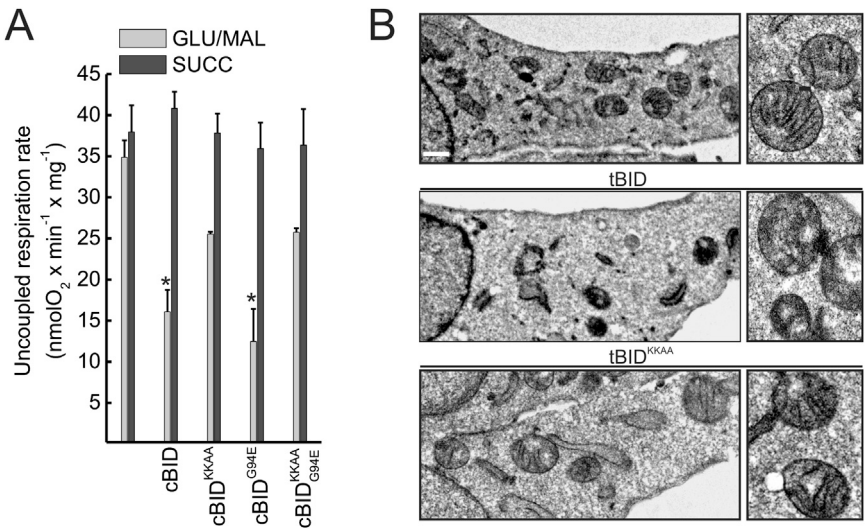

Figure S2. Cristae Remodeling Impairs Glutamate-Supported Uncoupled Respiration, Related to Figure 2

(A) Mitochondria isolated from mouse liver were treated with the indicated mutants of cBID for 10 min and 3uncoupled respiration rate was determined. Data represent average ± SEM of 3 independent experiments. *$p < 0.05$ in a pair sample Student's t test versus untreated.

(B) DKO MEFs were transduced as indicated and after 36 hr fixed and processed for electron microscopy. Bars, 1 μm (left) and 200 nm (right).

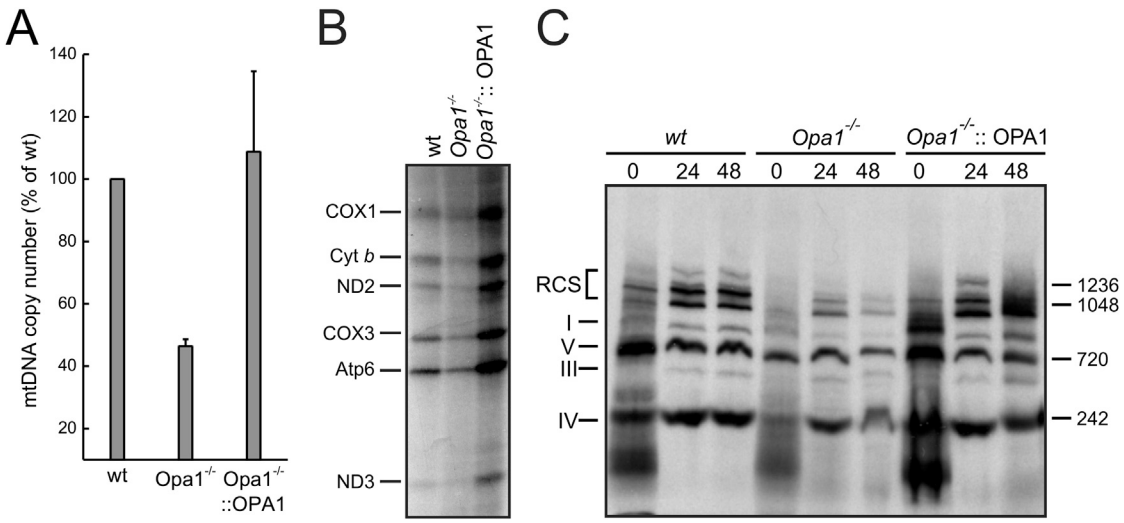

Figure S3. Chronic *Opa1* Ablation Causes Loss of mtDNA and Impairs mtDNA Translation, Related to Figure 3

(A) Mitochondrial DNA copy number quantification. mtDNA was amplified by RT-PCR from total DNA of the indicated cell lines using specific primers. The mtDNA copy number was normalized to the mtDNA copy number of the correspondent WT cell line. Data are average ± SEM of 5 dependent experiments. *$p < 0.05$ in a pair sample Student's t test versus WT.

(B) mtDNA translation assay. The indicated cell lines were metabolic labeled in presence of emetine and lysed after 30 min. Protein samples (40 μg) were separated by SDS-PAGE and the radioactivity was detected in the fixed and dried gels for 3 days. The mtDNA encoded proteins are indicated.

(C) RCS assembly assay. MEFs of the indicated genotype were metabolically labeled and chased for the indicated times. Equal amounts of protein (100 μg) were separated by BN PAGE and radioactivity was detected in the fixed and dried gels for 1 week. Individual complexes and supercomplexes of the respiratory chain are indicated.

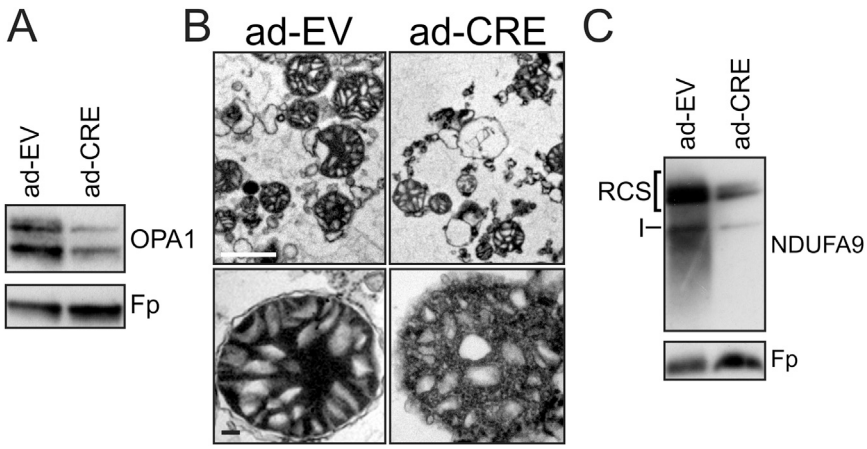

Figure S4. Acute Ablation of *Opa1* Affects Cristae Shape and RCS In Vivo, Related to Figure 4

(A) Levels of OPA1 in mitochondria from livers of *Opa1*$^{flx/flx}$ mice were isolated 3 days after tail-vein injection with the indicated adenoviruses. Protein samples (20 μg) were separated by SDS-PAGE and immunoblotted with the indicated antibodies.

(B) Representative electron micrographs of mitochondria isolated from livers of *Opa1*$^{flx/flx}$ mice 3 days after tail-vein injection with the indicated adenoviruses. Bars, 2 μm (top), 200 nm (bottom).

(C) BNGE analysis of RCS of mitochondria isolated from livers of *Opa1*$^{flx/flx}$ mice 3 days after tail-vein injection with the indicated adenoviruses. Equal amounts (100 μg) of proteins were separated in native conditions, transferred onto PVDF membranes and probed with the indicated antibodies. Individual complexes and supercomplexes of the respiratory chain are indicated.

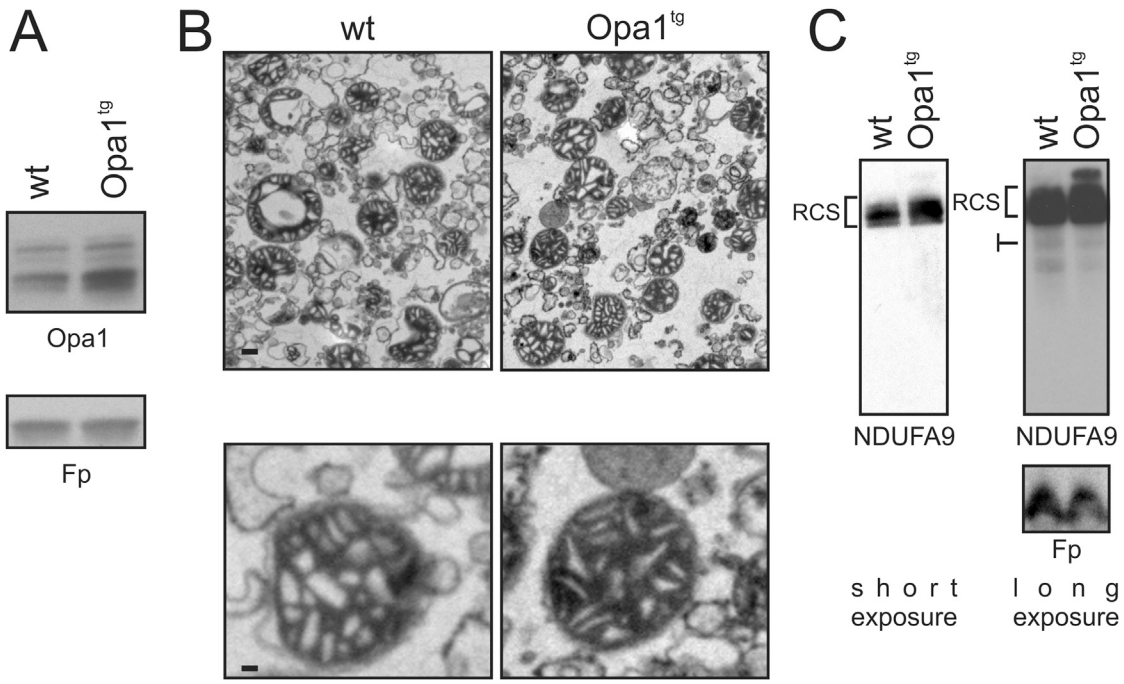

Figure S5. Overexpression of *Opa1* Decreases Cristae Width and Increases RCS In Vivo, Related to Figure 5

(A) Levels of OPA1 in mitochondria isolated from liver of *Opa1*^{tg} mice. Protein samples (20 μg) were separated by SDS-PAGE and immunoblotted with the indicated antibodies.

(B) Representative electron micrographs of mitochondria isolated from liver of *Opa1*^{tg} mice. Bars, 0.2 μm (top), 60 μm (bottom).

(C) BNGE analysis of RCS of mitochondria isolated from liver of *Opa1*^{tg} mice. Equal amounts (100 μg) of proteins were separated in native conditions, transferred onto PVDF membranes and probed with the indicated antibodies. Individual complexes and supercomplexes of the respiratory chain are indicated.

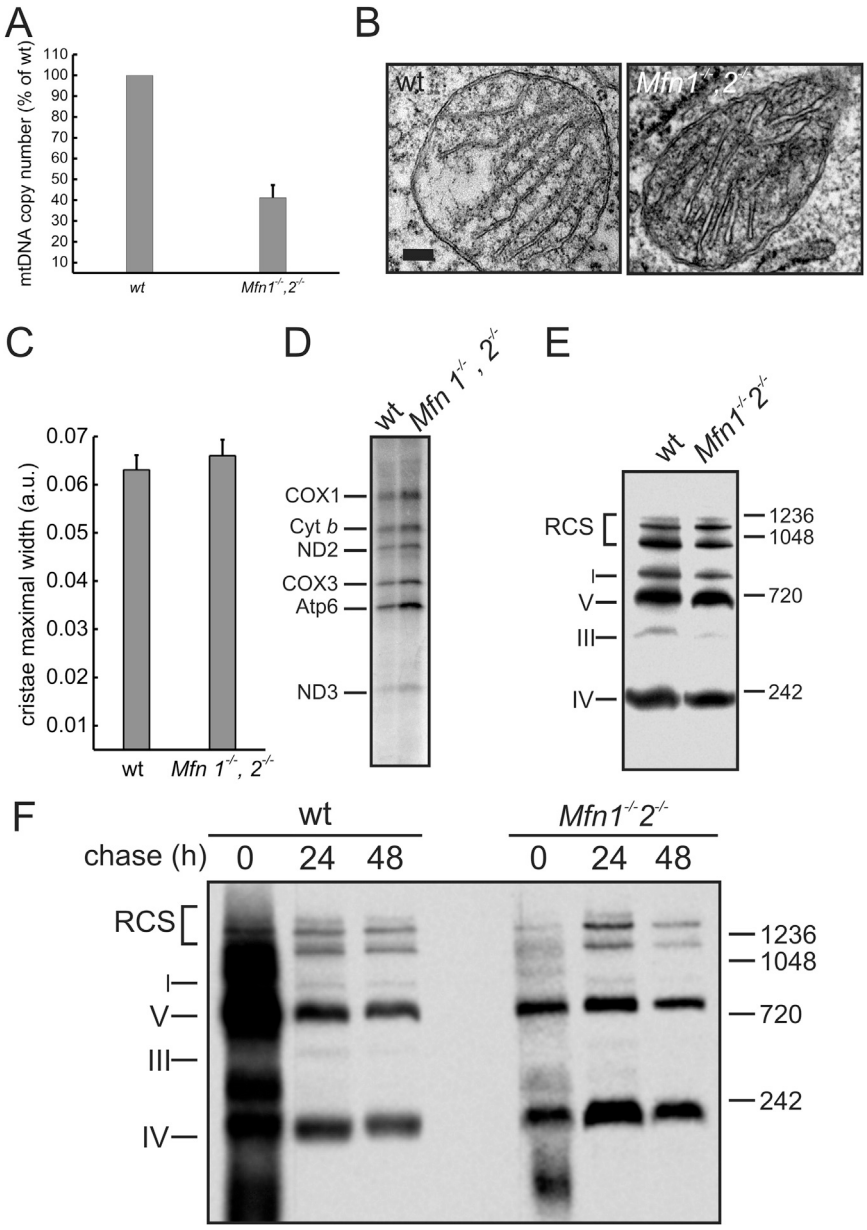

Figure S6. RCS Are Not Affected by Chronic Loss of *Mfn 1* and *2*, Related to Figure 6

(A) mtDNA copy number quantification. mtDNA was amplified by RT-PCR from total DNA of the indicated cell lines using specific primers. The mtDNA copy number was normalized to the mtDNA copy number of the correspondent WT cell line. Data are average ± SEM of 5 dependent experiments. *$p < 0.05$ in a pair sample Student's t test versus WT.

(B) Representative electron micrographs of cells of the indicated genotype. Bar, 500 μM

(C) Morphometric analysis of cristae width in mitochondria of the indicated genotype. Cristae width was measured in 40 randomly selected mitochondria. Data represent avarage ± SEM of 3 independent experiments.

(D) mtDNA translation assay. The indicated cell lines were metabolic labeled in presence of emetine and lysed after 30 min. Protein samples (40 μg) were separated by SDS-PAGE and the radioactivity was detected in the fixed and dried gels for 3 days. The mtDNA encoded proteins are indicated.

(E) BN PAGE analysis of RCS stability. MEFs of the indicated genotype were metabolically labeled. Equal amounts of protein (100 μg) were separated by BN PAGE and radioactivity was detected in the fixed and dried gels for 3 days. Individual complexes and supercomplexes of the respiratory chain are indicated.

(F) RCS assembly assay. MEFs of the indicated genotype were metabolically labeled and chased for the indicated times. Equal amounts of protein (100 μg) were separated by BN PAGE and radioactivity was detected in the fixed and dried gels for 1 week. Individual complexes and supercomplexes of the respiratory chain are indicated.